universität
wien

MASTERARBEIT

Titel der Masterarbeit

„Measurement and Simulation of the Interstrip Capacitance of Double Sided Silicon Sensors“

Verfasser

Bernhard Leitl, BSc

angestrebter akademischer Grad

Master of Science (MSc)

Wien, 2014

Studienkennzahl lt. Studienblatt:	A 066 876
Studienrichtung lt. Studienblatt:	Masterstudium Physik
Betreuerin / Betreuer:	Univ. Doz. DI Dr. Manfred Krammer

Dedicated to my parents
Maria & Gottfried

Abstract

The Insitute of High Energy Physics (HEPHY) at the Austrian Academy of Sciences (ÖAW) is involved in several research projects, including the Belle-II experiment in Tsukuba, Japan. The aim of this experiment is the investigation of the CP-violation of B-mesons. For this purpose electrons and positrons are collided in a storage ring. The particles created by these collisions are measured and analyzed by a detector.

The detector is divided into different specialized layers, to registrate the particles path and energy as accurate as possible. One of these detector layers will be the *Silicon Vertex Detector* (SVD), which is designed and made at HEPHY. The SVD is made of multiple layers of double-sided silicon sensors. As part of my master thesis, I developed a database system, to maintain all the sensors and components, needed for testing and constructing the SVD.

The sensors have strips on both sides, which are connected to readout chips to measure charges generated by a traversing particle. Due to the construction and operation of such a double-sided sensor, the strips on one side consist of p-doped (diode side) and on the other side of n-doped (ohmic side) silicon. However, since the base material (bulk) is n-doped, the strips on the ohmic side need a kind of insulation. The strip insulation used in this work, is based on p-doped areas implanted around the strips. This technique is called p-stop.

Part of my work was to investigate the impact of the p-stop geometry on the interstrip capacitance. This is of special interest since the interstrip capacitance is directly related to the signal-to-noise ratio of the sensor, which is an important quality characteristic. These measurements showed an interesting relationship between the interstrip capacitance, and the distance from the strip to the p-stop. The fit function of this relationship, was different for each tested geometry.

Furthermore, I tried to develop a model by using an analog electronic circuit simulator, explaining the observed measurements.

Kurzfassung

Das Institut für Hochenergiephysik (HEPHY) der Österreichischen Akademien der Wissenschaften (ÖAW) ist an mehreren Forschungsprojekten im Bereich der Teilchenphysik beteiligt, unter anderem auch am Belle-II Experiment in Tsukuba, Japan. Dieses Experiment dient zur Erforschung der CP-Verletzung von B-Mesonen. Dazu werden in einem Speicherring Elektronen mit Positronen zur Kollision gebracht und die dabei entstehenden Teilchen in einem Detektor registriert und bestimmt.

Der Detektor ist in verschiedene hochspezialisierte Schichten unterteilt um eine präzise Erfassung der Bahn und Energie eines Teilchens zu ermöglichen. Eine dieser zukünftigen Detektorschichten ist der *Silicon Vertex Detector* (SVD), welcher am HEPHY entwickelt und konstruiert wurde. Der SVD ist ebenfalls aus mehreren Schichten doppelseitiger Silizium-Sensoren aufgebaut. Um diese Sensoren und all die noch zusätzlich benötigten Komponenten verwalten zu können, habe ich im Zuge meiner Masterarbeit ein Datenbanksystem entwickelt.

Auf beiden Seiten des Sensors befinden sich Streifen, an welchen die beim Durchgang eines geladenen Teilchens erzeugten Ladungen, durch spezielle Chips gemessen werden. Aufgrund der Konstruktion und Funktionsweise solch eines doppelseitigen Sensors, bestehen die Streifen auf einer Seite aus p-dotiertem (Diodenseiten) und auf der anderen aus n-dotiertem Silizium (ohmsche Seite). Da allerdings das Grundmaterial (bulk) n-dotiert ist, muss auf der ohmschen Seite eine Isolation zwischen den Streifen erzeugt werden. Als Streifenisolation dient ein p-dotierter Bereich, p-stop genannt, welcher die Streifen umschließt und elektrisch voneinander trennt.

Teil meiner Arbeit war es die möglichen Geometrien hinsichtlich ihres Einflusses auf die Kapazität zwischen den Streifen zu untersuchen. Dies ist vor allem von Interesse, da diese Kapazität direkt mit dem Signal-Rausch-Verhältnis des Sensors in Zusammenhang steht, welches ein wichtiges Qualitätsmerkmal ist. Diese Messungen zeigten einen interessanten Zusammenhang zwischen der Kapazität und dem Abstand vom Streifen zum p-stop, welcher je nach Geometrie durch eine andere Funktion beschrieben wird.

Weiters versuchte ich mittels einer Software zur Simulation analoger elektrischer Schaltungen ein Modell zu entwickeln, um die beobachteten Ergebnisse zu erklären.

Contents

1 The Belle experiment and its upgrade

1.1 Physical motivation

The standard model (SM) of particle physics is a theory describing the basic forces of nature by the interactions of fundamental particles. Those particles are categorized by their charge, mass and spin into different groups shown in figure 1.1.

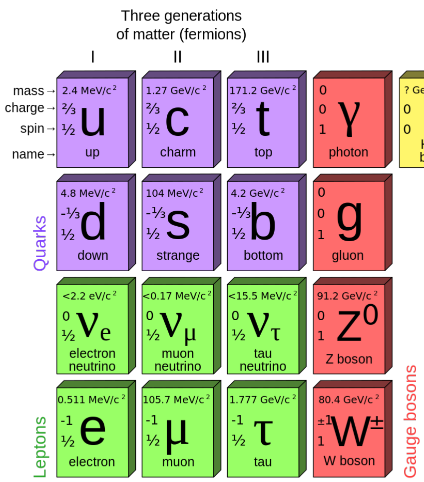

Figure 1.1: Overview of the fundamental particles of the standard model [1]

There are two main species of particles:

- Fermions, which are the building blocks of matter and
- Gauge bosons, which are exchange particles and therefore responsible for the weak, strong and electromagnetic force.

Fermions are again divided into two groups, which are called leptons and quarks. Quarks only occur in groups of two (mesons) or three (baryons) and cannot exist independently, in contrast to leptons. Every particle has its own antiparticle.

If the Big Bang produced matter and antimatter in the same amount, why didn't they annihilated each other? The answer is, one or more physical processes must work differently for matter than for antimatter. In 1955 Wolfgang Pauli described one of the fundamental physical laws, the CPT-theorem. It states that physical laws are invariant under a simultaneous transformation of charge, parity and space called CPT-Transformation. This means, that every process which can be produced by replacement of particles with anti-particles (charge inversion), swapping space directions and reversion of time, is possible and in accordance with physical laws. Although the CPT-symmetry is proven to be true by experiments with todays possible accuracy, it does not have to be true for the transformation of its components. In 1964 one of the most important facts for the understanding of weak interactions in particle physics was revealed.

The observation of rare decays of neutral kaons showed a violation of the CP-symmetry. Not only the Belle group gained this result also the analysis of the American counterpart, the BaBar [2] experiment, revealed this phenomenon. Both experiments confirmed the predictions of M. Kobayashi and T. Maskawa [3], which were honored in 2008 with the Nobel Prize in Physics.

The CP violation, could be one of the reasons for the imbalance between matter and antimatter. But further investigations are necessary, because the observed violation is many orders of magnitude too small to explain the whole matter dominance.

Nevertheless the discovery of this symmetry break is very important for the understanding of weak interactions in particle physics.

1.2 KEKB and the Belle experiment

The Belle detector is located at the High Energy Accelerator Research Organization (KEK) in Tsukuba, Japan. The name is a reference to the measured B-mesons (B), which have their origin in the collisions of electrons (el) and their anti-particles (le). The experiment is an international collaboration of over 400 physicist and engineers studying B-physics, especially the CP-violation of B mesons. It is the only experiment running on the KEKB accelerator, which is an asymmetric electron-positron collider (electron 8GeV, positrons 3.5GeV). To generate a high number of B mesons it is operated near the $\Upsilon(4S)$ resonance. Between 1999 and 2010 the detector collected an integrated luminosity of about $1.04ab^{-1}$, corresponding to more than a billion $B\overline{B}$ pairs.

1.3 SuperKEKB and Belle II

The SuperKEKB accelerator (figure 1.2) is the new upgraded and refurbished version of KEKB. The aim of the upgrade is to gain a 40 time higher luminosity which should be in total $8 \times 10^{35} cm^{-2} s^{-1}$. The changes on the accelerator also require a redesign and reconstruction of the Belle detector, the new detector is called Belle II (figure 1.3).

The much higher beam luminosity and the very small interaction region of about 10 mm will increase the beam-related background. Therefore the hit rates, directly around the beam, will reach a level, which is way to high to be dealed with strip

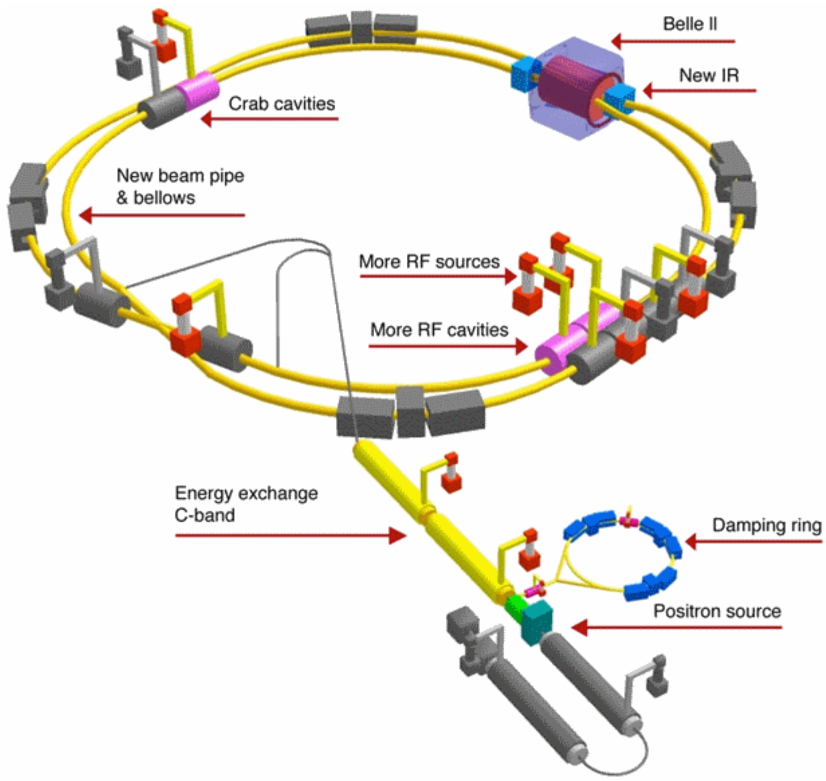

Figure 1.2: The new SuperKEKB collider. [4]

detectors. The assumed occupancy [1] for strip detectors near the beam pipe would be unacceptable. With too many channels giving a signal, it is difficult to differ between signals from the background and those belonging to the triggered event. So a reconstruction of any vertex would be impossible. To get rid of this problem there are two solutions:

- Increase the number of channels by reducing their size, with the disadvantage of higher production costs.
- Increase the readout frequency of each channel by reducing the shaping time, at the cost of the signal-to-noise ratio.

The new vertex detector will use both approaches to improve performance. For the innermost layers the second approach was not practicable, so they will be replaced by a two-layer silicon pixel detector. But for radii beyond 40 mm, strip detectors will work safely and benefit from new readout chips with much faster shaping times. Therefore the layers will be shifted towards higher radii, resulting in a bigger detector volume, which in turn improves the reconstruction efficiency of K_S decays.

[1] Occupancy provides information about the mean number of channels over threshold.

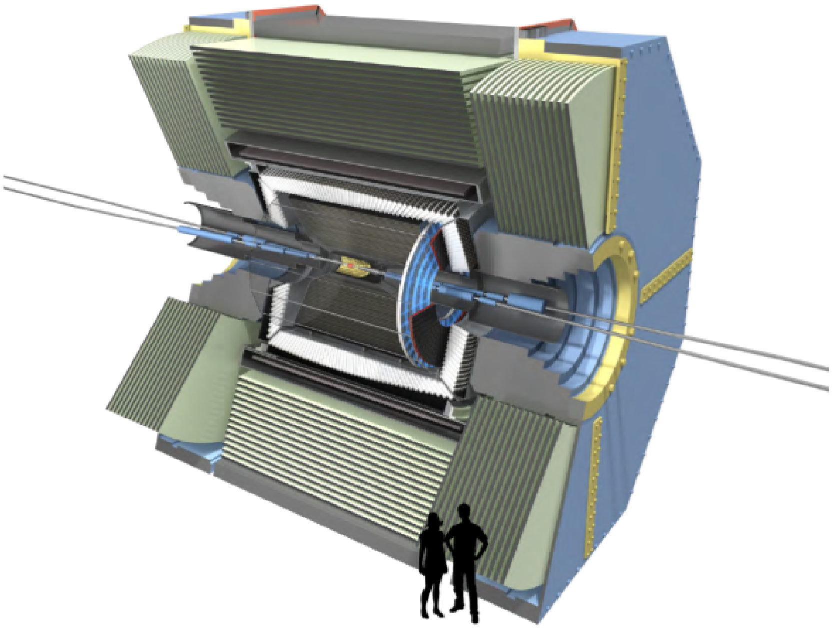

Figure 1.3: The new BelleII detector. [5]

Other important improvements of Belle II are:

- Reduced size of the drift cells in the central drift chamber (see section 1.4.3) will improve the tracking reconstruction.
- A completely new particle identification device, capturing photons emitted by Cherenkov radiation, will collect additional data improving the pion/kaon separation.
- The endcaps of the muon KL detector will be replaced by scintillators equipped with photomultipliers.

1.4 Detector design

1.4.1 Pixel Detector (PXD)

As mentioned before, the first two detector layers at radii of 1.4 cm and 2.2 cm are forming the PXD. An important issue for the reconstruction of B-decays, is multiple scattering. This happens, because a charged particle passing through matter interacts with the Coloumb field of the nuclei. Usually the particle mass is much smaller than those of the nuclei, so the resulting deflection of the particle is small. But if the particle gets scattered multiple times, its path change will not be negligible. This additional random path component, would significantly reduce the precision of the vertex reconstruction.

At the SuperKEKB collider this issue becomes even more significant, because it is running at relatively low energies. To reduce multiple scattering, the matter inside the active detector volume has to be limited to the necessary minimum. This is one of the reasons why the PXD will use DEPFET (DEPleted Field Effect Transistor) technology, which allows a very thin sensor design ($50\mu m$). An additional advantage is, that the pixels are only "on" during readout, this results in a low power consumption, allowing an operation without any extra cooling system. Also the possibility to place its readout electronics and its cooling devices outside the active detector volume will help to keep the material budget at a minimum. The pixel detector has a very good spatial resolution, due to the small cell sizes of 50µm × 50µm for the first layer and 50µm × 75µm for the second layer, respectively.

Before a technology can be used inside a detector, its radiation hardness has to be proven. This is a very important criteria for a stable long term run. But irradiation tests have shown, that it is possible to produce radiation hard DEPFET pixels, so this should not be a problem.

DEPleted Field Effect Transistor (DEPFET)

1990 the first working DEPFET detector was engineered and proved the predictions of Josef Kemmer and Gerhard Lutz, which invented the working principal of this technology back in 1987 [6]. With this devices it is possible to detect charged particles.

Figure 1.4 shows a schematic view of a single DEPFET. The central unit is a p-channel MOSFET (metal-oxide-semiconductor field-effect transistor). If a particle passes the full depleted n-Si bulk, it generates electron-hole pairs. Due to the applied depletion voltage the positive holes are drifting to the negative charged back side of the detector, while the electrons are attracted from the potential minimum generated by the internal gate. The internal gate is a highly n-doped area approximately $1\mu m$ underneath the external gate. By applying a voltage to the gate it is possible to activate/deactivate the cell. If the cell is on, the charges accumulated by the internal gate, have an direct effect on the conductivity of the MOSFET (resistance between source and drain). A measurement of the conductivity provides information about the amount of electrons generated by the

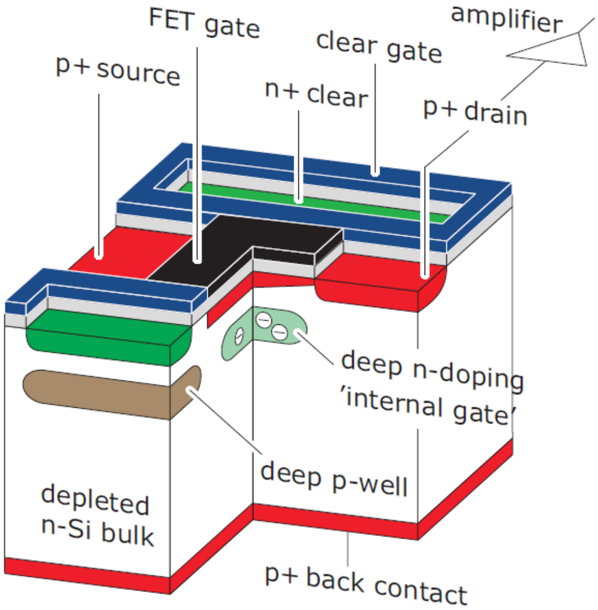

Figure 1.4: Cross-section of one DEPFET cell. [7]

particle. This allows conclusions about the energy of the incident particle. Thanks to the amplification of the MOSFET, directly above the charges origin, lateral losses can be compensated. The readout can be repeated many times, because the signal charges remain at the internal gate. This can be used to reduce statistical fluctuations. Removing the charges from the internal gate is initiated by pulsing the n+ doted "clear" contact. This resets the cell and prepares it for the detection of a new particle.

Another advantage of the DEPFET is the very low noise level, due to the very small capacitance of the internal gate [7].

1.4.2 Silicon Vertex Detector (SVD)

A detailed explanation of the SVD will be given in chapter 2.

1.4.3 Central Drift Chamber (CDC)

A CDC is able to detect a particle by measuring the amount of ions generated by the particle while traversing through a chamber filled with gas.

One has to differ between direct/primary and indirect/secondary ionization. It is called direct ionization when a particle with high kinetic energy hits an atom or molecule liberating an electron. A photon can also cause atoms to ionize directly through the compton or photoelectric effect, but electrons released by one of these effects have so high energies that they in turn can ionize atoms. This ionizing process is called indirect or secondary ionization. To prevent electrons and ions to recombine with each other, a electrical field needs to be applied, which separates those charge carriers. A very simple realistation of a proportional counter is shown in figure 1.5.

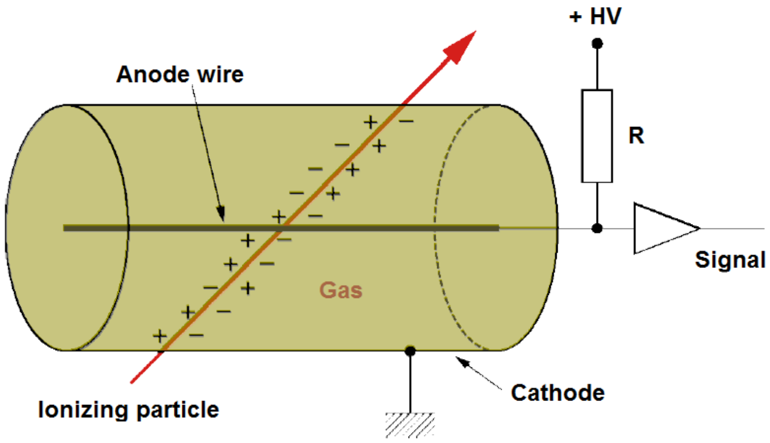

Figure 1.5: Schematic view of a proportional counter. [8]

The image shows a cylindrical shaped chamber filled with a gas, which gets ionized by an incident particle. Through the center runs a wire, which is on both ends electrically insulated from the chamber. This is necessary, because in this approach the chamber is used as cathode and the wire as anode. A high voltage applied between both elements creates a electromagnetic field which in turn causes the electrons to move towards the wire. Near the wire the field increases so much, that the kinetic energy of the electrons is sufficient to ionize more atoms by hitting them. This effect amplifies the end signal, which is very important, because the average energy loss for a particle moving through gas is about 1 keV/cm and the energy needed to ionize a particle is about 30 eV. So approximately 30 electron ion pairs are generated by a particle per centimeter. This alone would be way to small for inducing a good readout signal.

A very important characterisitic of the amplification is its proportionality to the applied voltage. This allows conclusions about the amount of primary generated charges and thereby the energy of the detected particle. A set of alternating horizontal stretched anode wires and vertical cathode wires, assigns also a spatial resolution to the signal. With additional wires it is possible to form the electrical field in such a way, that it is possible to estimate the average drift velocity of the ions. With very accurate time measurements of the current pulses induced into the wires and the knowledge of the time it took the ions to drift to the wire, very precise conclusions of their origin are possible. Detectors using this technique are called drift chambers.

The central drift chamber for Belle II has to fullfill three important tasks:

- Track reconstruction and precise momenta measurements.
- Determine energy losses as additional information for particle identification
- Collecting trigger signals for charged particles

The CDC will consist of an inner and an outer carbon-fiber reinforced plastic (CFRP) cylinder. The outer cylinder has a thickness of about 5mm and must hold about 4 tonnes of wire tensions. Because of material budget considerations the inner cylinder has only a thickness of 0.5mm, which should be sufficient to support the wire tensions for the small chamber. Aluminum endplates will increase the strucutral stability of the detector and minimize deformations caused by wire tensions.

The chamber will be filled with a gas mixture of 50% helium and 50% ethane, the same mixture used for Belle. No other mixture has until now shown a better performance.

1.4.4 Electromagnetic Calorimeter (ECL)

The barrel of the electromagnetic calorimeter will be 3m long with a radius of 1.25m. Together with the endcaps it will contain 8739 CsI crystals with a total weight of 43 tons. Each sensor is equipped with two photodiodes at the rear end, for scintillation light detection. An attached LED can send light pulses into the crystal for testing and calibration purposes. A water cooling system and dry air will ensure a stable operating temperature and low humidity.

1.4.5 Kaon and Muon Detection System (KLM)

As the name of this system suggests the main task of this unit will be the detection of kaons, especially the K_L^0 meson, and muons with a momentum of at least 0.6 GeV/c. The KLM is placed outside the superconducting solenoid. The barrel region is composed of alternating iron plates and glass-electrode resistive plate chamber (RPC) modules. Each iron plate is 4.7 cm thick and provides at least 3.9 interaction lengths for the K_L^0 meson. This will ensure that also the very weakly interacting K_L^0 meson will be absorbed and shower hadronically before escaping the detector. For Belle also the endcapes were equipped with RPCs, due to the higher background of Belle II this is not possible anymore. Therefore the RPCs get replaced by a scintillator strip detector. Wavelength-shifting fibers connect the scintillators to multipixel silicon photodiodes, which are able to operate even in the strong magnetic field of the solenoid.

The muon reconstruction consists mainly of two steps. In the first step each track identified by the CDC with a momentum larger than 0.6 GeV/c is extrapolated into the region of the KLM, under the hypothesis, that it is a pion. As mentioned before 0.6 GeV/c are needed to reach the KLM. The predicted range is defined as the last layer hit by the extrapolated track. All detected hits near the extrapolated track are associated with it. If the last found hit differs too much from the predicted range the track gets considered as hadronic and is rejected. All not rejected tracks are passed to the second step. Now each track is extrapolated again, but in this case with the muon hypothesis. The accordance of the predicted and measured range as well as the goodness of the fitted track, are used for the likelihood ratio to determine the probabilty that the track belongs to a muon rather than to a charged hadron.

The kaon finding algorithm groups all hits to clusters by spatial criterias. Then for each track the angle between its entrance point and the cluster centroid (starting from the interaction point) is calculated. If it is smaller than 15° the cluster is discarded. All not discarded clusters are treated as K_L candidates, if they can be associated with a neutral ECL cluster. This is possible if they are within a 15° angle of each other. The final cluster direction is the one reconstructed by the ECL.

2 The Silicon Vertex Detector (SVD)

2.1 General

The SVD detects particles by their generated charges (e^-h^+-pairs) on their way through silicon sensors. The amount of such generated charge carriers is direct proportional to the energy loss of the passing particle (see section 3.1.4). For position information the sensor surface is divided into strips. The strip nearest to the traversing particle gives a higher signal than more distant ones. In combination with perpendicular strips on the other sensor side it is possible to gain a 2D space resolution of a few μm. A sensor with readout strips on both sides is called a double sided strip detector (DSSD) and will be discussed in detail later in chapter 3. These DSSDs are arranged in multiple layers around the IP. Each layer detects the coordinates of the hit, so it is possible to calculate the path of the particle through the detector.

2.2 The limits of the previous Silicon Vertex Detector (SVD2)

The previous version of the Belle I experiment, the SVD2, was installed in 2003. It has been succesfully operated over 7 years until its shutdown in 2010. It had four concentric layers composed of double sided silicon sensors, made of 4" wafers. Each sensor was assembled with two others and connected to a VA1TA chip for read out. The combination of this elements is called ladder. The VA1TA had a peaking time of 800ns, which was sufficient for the planned luminosity at the beginning of the project. As it turned out, at the end of the Belle experiment, with higher luminosities the occupancy became one of the limiting factors for efficient tracking.

Figure 2.1 shows an estimated hit occupancy of the SVD2 for the simulated SuperKEKB environment. The 40 times higher luminosity of SuperKEKB would raise the occupancy to an unacceptable level. This is the reason, why the vertex detector needed a complete redesign.

To reach a lower occupancy the new SVD needs a new readout chip with a very short shaping time, pipelined read out and a faster clock speed.

Even with all these improvements the detecor will not be able to handle the amount of particles directly around the beam pipe. Therefore the first layer will be realized by a pixel detecor as described in section 1.4.1. Although the PXD offers a very high spatial resolution it has a rather long integration time of $20\mu s$. Furthermore a particle detection system for the whole volume realized only by pixel

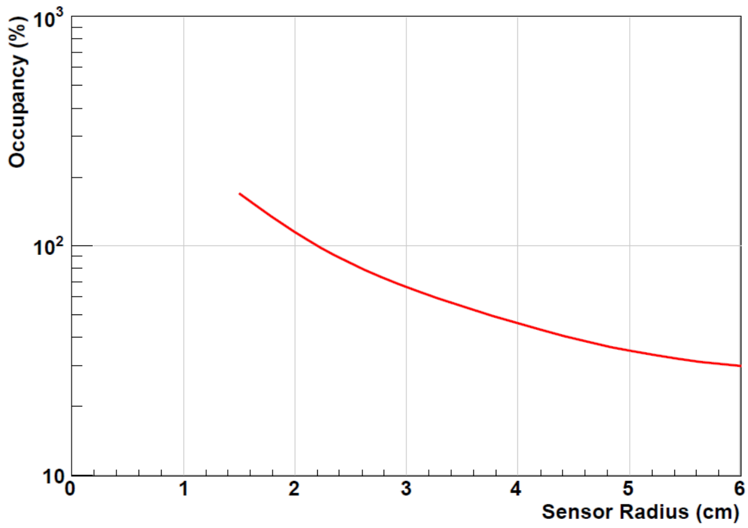

Figure 2.1: As shown in the *Belle II technical design report (2010)* [7], the simulated occupancy of the old SVD2 expected for SuperKEKB. The active sensor size was assumed to be $2.5 \times 7.5\text{cm}^2$ and 800ms as shaping time, the time of the VA1TA readout chip.

detectors would be to expensive and imply an unmanageable amount of channels. For this reason the Belle II SVD will be constructed to link the measured tracks by the PXD to the ones reconstructed from the CDC. This should guarantee a high efficient reconstruction of the B decay vertices. Important for the determination of CP violating asymmetries, induced by particle-antiparticle mixing. Furthermore the refurbished detector will also be able to track vertex information of the D-meson and τ-lepton decay channel.

2.3 The new SVD

2.3.1 Construction

In the last years, progress has been made by the silicon manufacturers, which makes it possible to fabricate double sided sensors on six-inch wafers. Because of that fewer sensors, readout electronics and cooling equipment is needed to equip the same volume compared with the old SVD. The new SVD design surely benefits from this improvement, in lowering the needed material budget.

187 sensors are going to be assembled to 49 ladders. In turn, these ladders will be arranged in four concentric layers around the beam pipe (fig. 2.2). Those layers are planned to be at radii of 38 mm, 80 mm, 115 mm and 140 mm. Table 2.1 lists the amount of sensor and readout chips, used for each layer.

Another interesting detail is the new geometric shape. The layers of the old SVD were arranged like concentric cylinders. Due to the larger layer radii of the new SVD, this layout had to be changed. Especially for the forward part additional sensors would be required to cover the whole acceptance range of $17 < \theta < 150$, where θ is the angle taken from the beam axis. For this reason the front region is shaped conical. This also leads to a steeper angle for the traversing particles, and in turn to a better spatial resolution. Trapezoidal sensors have been designed to fullfill the requirements for this individual geometry. Furthermore the detector design takes care of the mechanical stability and an high efficient integrated CO_2 cooling system [9]. The overall scheduled material budget per DSSD ladder will be 0.57% per radiation length. The DSSD sensor alone contributes 0.32% [7].

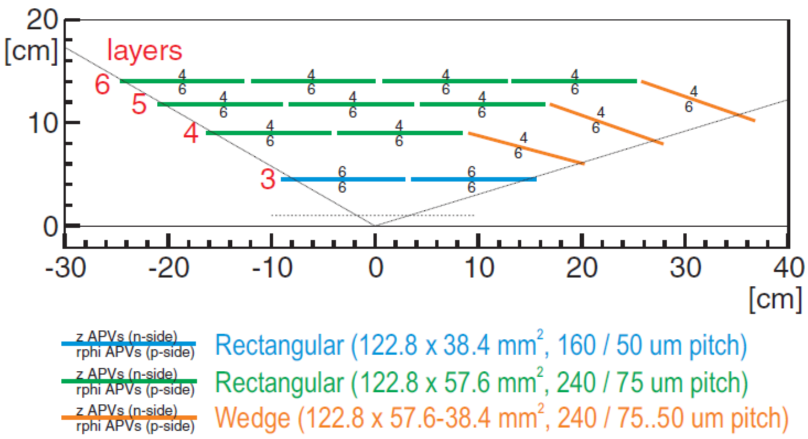

Figure 2.2: Schematic presentation of the four SVD layers. The three sensor geometries are shown in different colors. The numbers on the top and down side give the corresponding amount of planned readout chips [7].

On account of the larger layer radii the Belle II SVD will have a slightly larger volume, compared to the SVD2 and with $1.24\,\mathrm{m}^2$ nearly twice of the active area. Three different sensor layouts are needed to obtain an optimal arrangement of the sensors. The dimension of the sensors in the first layer of the barrel region is 122.8×38.4 mm^2 with a 160 µm pitch on the n-side (top) and 50 µm on the p-side (bottom). The sensors in the outer three layers are a little bit larger 122.8×57.6 mm^2 and have a pitch of 240 µm (n-side) and 75 µm (p-side). The trapezoidal sensors for the slanted forward region are 122.8 mm long and due to their shape one side is 57.6 mm and the other one only 38.4 mm wide. The pitch on the n-side is the same as the one from the larger rectangular sensors 240 µm, but on the p-side the pitch varies between 75 µm to 50 µm. The strips on the p-side (junction side) are running parallel to the long edge of the sensor and are therefor longer than the vertical orientated strips on the side n-side (ohmic side).

All sensors are mounted on the ladder with their p-side facing the interaction point so that the strips on the p-side are parallel to the beam axis.

In sum over 1900 readout chips with a fast shaping time of O(50 ns) are needed

Layer	Radius (mm)	Ladders	Sensors/ladder	Sensors	Readout chips/sensor	Readout chips
6	140	17	5	85	10	850
5	115	14	4	56	10	560
4	80	10	3	30	10	300
3	38	8	2	16	12	192
Sum		49		187		1902

Table 2.1: The layer numbering starts with 3 on account of the first two PXD layers [7].

[7]. After some research the APV25 [10] was chosen. It was originally developed for the CMS silicon tracker, where it has shown a very reliable performance. Detailed tests were done on the APV25. Showing that it is radiation hard up to an integrated dose of 30 MRad [7]. Also its ability for pipelining and the analog readout scheme are perfectly suitable for the use in the Belle II SVD. Due to its fast shaping time the input capacitance needs to be small to reduce noise effects. The main contribution to the input capacitance comes from the connection length between sensor and the readout chip. For this reason the APV25 will be mounted directly on the DSSDs.

3 The double sided silicon sensors

3.1 Semiconductors

Materials can be divided by there electrical conductivity into those which are able to transport electrical charges - conductors - and those who are not - insulators. But there is also a third group called semiconductors, permiting the transport of electrical charges, but with a much lower conductivity than that of a normal conductor. Energy bands are a model originating from quantum phyiscs. The Pauli exclusion principle says that each quantum state of an atom can only be occupied by one electron at the same time. Each state is associated with an energy level. The lower energy levels are filled first, but only the higher levels contribute to the electrical conduction. The levels of a single atom are discrete, but if two or more atoms are close to each other they split up. In a crystal with lots of atoms the energy levels are so close to each other that they can be grouped to continous energy bands. Electrons can not occupy energy levels between those bands.

The band containing the highest occupied states is called the valence band, while the superposition of the lowest unoccupied states form the conduction band. As long as the valence band is fully filled with electrons and the conduction band is empty, no electron transport is possible. For this reason some electrons must be lifted from the valence- to the conduction band. The energy needed to transfer an electron is called E_G and represents the difference between the lower bound E_C of the conduction band and the upper bound E_V of the valence band.

$$E_G = E_C - E_V \tag{3.1}$$

The width of the gap influences the electrical behaviour of the material. If there is no gap or even an overlap of the two bands the material is called a conductor. Semiconductors have a small E_G, so electrons from the valence band are more likely to cross the band gap, increasing the number of partially filled states. For insulators E_G is very high ($E_G > 4eV$), nearly no electrons can move to the conduction band, even at higher temperatures.

3.1.1 Doping

Impurities in the silicon crystal can have an significant impact on its conductivity properties. A controlled process of introducing foreign atoms is called doping. Depending on the atom type introduced into the silicon crystal, it is called n-type or p-type semiconductor. N-type uses donor dopands and p-type acceptor dopands.

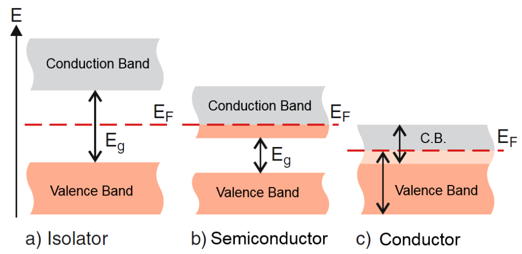

Figure 3.1: Band gaps of different materials. [11]

The difference between those elements is their number of valence electrons available for covalents bonds. Silicon has 4 valence electrons, acceptor dopands only three and donors five. When an acceptor atom substitutes a Si atom in the crystal lattice it bonds with three of its neighbour atoms leaving one neighbour unsatisfied. A neighbouring electron can repair the bond by changing its position, but leaving a hole on its previous position. Soon another electron will be attracted by the hole and replaces the missing electron. This leads to a moving hole, which can be interpreted as a positive charge carrier. Donor atoms increase the amount of available electrons for charge carrying, because only four of the five valence electrons are bonded. The fifth one is only weakly bonded, even room temperature provides enough thermal energy to liberate it from its donor atom. The liberated electrons can move freely through the crystal and contribute to the electrical conduction.

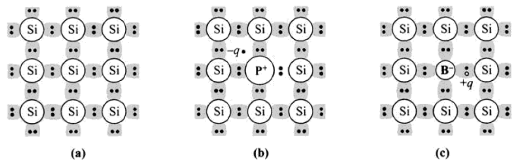

Figure 3.2: The three different Si bondings. (a) showing a pure Si crystal. (b) showing a n doped Si crystal with phophorus as donor. (b) p-type doping with boron as acceptor. [12]

The Fermi level E_F represents the energy level at thermal euqilibrium with an occupation probability of 50 %. The occupation probabilty of a given energy level ϵ is given by the Fermi-Dirac distribution [12] $f(\epsilon)$ as equation 3.2 shows, with T as the absolute temperature and k the Boltzmann's constant.

$$f(\epsilon) = \frac{1}{e^{(\epsilon - E_F)/kT} + 1} \tag{3.2}$$

Doping influences the position of the Fermi level within the band gap. P-type doping shifts the Fermi level toward the valence band, respectively n-type causes the opposite.

3.1.2 pn-junction

A pn-junction is a structure composed of a p and n-type material. The simplest component of this kind is a pn-junction diode (figure 3.3).

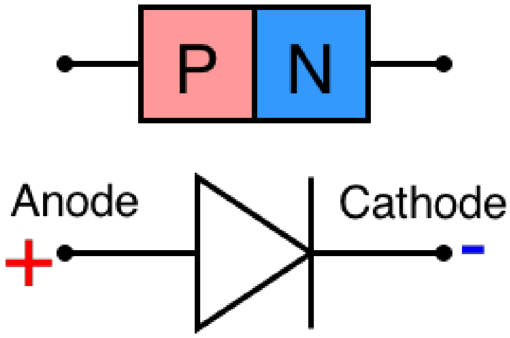

Figure 3.3: The junction diode and its schematic symbol.

When connecting a battery with its positive terminal to the p-type and the negative to the n-type end of the diode, a current flow can be measured. The diode is called to be forward biased. Interchanging the voltage connections, will result in a nearly blocked current flow. The diode is now reverse biased.

To understand this behaviour it is important to know how currents flow through a semiconductor. There are two processes which are responsible for the current flow: drift and diffusion. As explained before the electrons and holes introduced by the dopands can freely move around. They always try to achieve a homgeneous distribution over the whole volume. For this reason regions with high electron or hole concentration spread out until they reached a more uniform state. This process is called diffusion. An electric field applied to a semiconductor will attract the electrons to the positive and the holes to the negative potential. This is called drift. A diode is a structure of two very concentrated charge carrier regions. The holes of the p-side will try to diffuse to the n-side and vice versa the electrons of the n-side will try to move to the p-side (figure 3.4). At the beginning both regions are electrically neutral, but donor atoms which get seperated from their diffusing electrons become positive charged ions. The same is true for the acceptor atoms in the p region, which become negatively charged, because the diffusing electrons recombine with the holes. The positive ions on the n-side and the negative ions on the p-side create a potential, which counteracts the diffusion of electrons and holes. This potential is also called barrier voltage or contact potential. The pn-junction is in euquilibrium or steady state, if the currents drift component, build up by the barrier voltage, exceeds the diffusion component. A so called depletion zone between p and n-type semiconductor arises, which is nearly depleted from free charge carriers.

The width of the depletion zone can be manipulated by applying a voltage to the diode. Reverse biased, the depletion zone expands, which further decreases

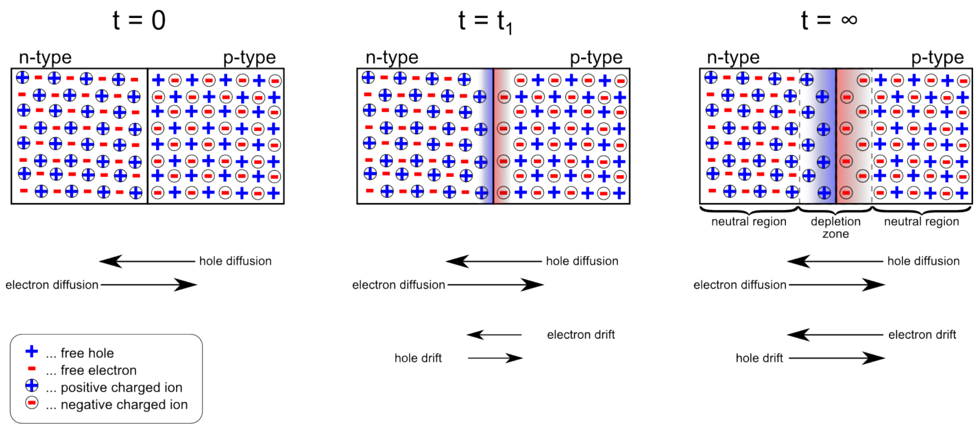

Figure 3.4: Diffusion process of the electrons and holes to the opposite region building up the depletion zone.

the amount of mobile charge carriers. Only a very small reverse current can flow. Forward biased, the depletion zone decreases. If the applied voltage exceeds the barrier voltage, the diode get conductive and a large current can flow.

3.1.3 Principle of operation

At first the sensor must be depleted of intrinsic charge carriers. Therefore a reverse bias voltage is applied to the sensor generating a depletion zone. The voltage must be high enough to expand this charge carrier free zone over the whole sensor thickness. If a charged particle hits a silicon atom it can ionize this atom by lifting an electron to the conduction band. As explained earlier the electron leaves a hole in the valence band, which can be treated as a positive charge carrier. Electrons and holes are always created in pairs, the so called e-h-pairs. On its way through the sensor a particle generates many of such e-h pairs depending on the particles energy loss and the minimal amount of energy needed to create such pairs. Due to the applied bias voltage the electrons are attracted to the ohmic side and the holes to the negative diode side. This charge flow induces a current into the p-strips and n-strips, which is measured by the attached readout electronics. The readout electronic is capable of determining the amount of created e-h-pairs, this allows conclusions about the particles energy loss, which is helpful for particle identification.

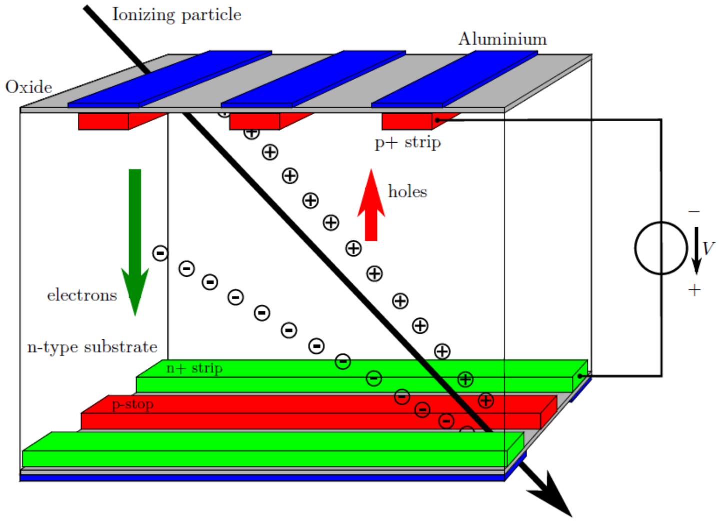

Figure 3.5: The particle detection principle of a doublesided silicon sensor. [13]

3.1.4 Particles energy loss

The amount of generated e-h-pairs of a traversing particle is direct proportional to its energy-loss. The mean energy loss of a heavy particle traversing a material, is described by the Bethe-Bloch equation [14]:

$$-\left\langle\frac{dE}{dx}\right\rangle = Kz^2\frac{Z}{A}\frac{1}{\beta^2}\left[\frac{1}{2}\ln\frac{2m_ec^2\beta^2\gamma^2T_{max}}{I^2} - \beta^2 - \frac{\delta(\beta\gamma)}{2}\right] \tag{3.3}$$

This equation is only applicable for heavy particles with a mass of a muon or larger m_μ and a relativistic velocity between $0.05 < \beta\gamma < 500$. Figure 3.6 shows the graph of the Bethe-Bloch equation for muons in copper. As can be seen the function reaches a minimum at about $3\beta\gamma$. Particles with about this energy are called "Minimum Ionising Particles" (MIPs).

For electrons and positrons the Bethe-Bloch equations needs an adaption, because now the incident particle and the target electron have the same mass. Also note that scattering of two e^- is a process between two identical, undistinguishable particles, so one has also to differ between positrons and electrons at low energies. The modified Bethe-Bloch equation describing the mean energy loss for an electron with kinetic energy T through ionisation is [14]:

$$-\left\langle\frac{dE}{dx}\right\rangle_{el.} = K\frac{Z}{A}\frac{1}{\beta^2}\left[\ln\frac{m_ec^2\beta^2\gamma^2T}{2I^2} + F(\gamma)\right] \tag{3.4}$$

Another very important contribution for the energy loss of electrons in a medium is bremsstrahlung (see fig. 3.7). Bremsstrahlung arises if a charged particle gets accelerated by the coloumb field of a nucleus. A very important characteristic parameter in this context is the radiation length (eq. 3.5). It describes the average

Symbol	Definition	Unit or Value
K/A	$4\pi N_A r_e^2 m_e c^2/A$	$0.307\,075\,\mathrm{MeVg^{-1}\ cm^2}$ for $A = 1\,\mathrm{g\,mol^{-1}}$
N_A	Avogadro constant	$6.0221415 \times 10^{23}\ \mathrm{mol^{-1}}$
r_e	Classical electron radius $e^2/4\pi\epsilon_0 m_e c^2$	$2.817\,940\,325(28)\,\mathrm{fm}$
$m_e \times c^2$	Electron mass $\times c^2$	$0.510\,998\,9\,\mathrm{MeV}$
A	Mass number of medium	Si: 28
Z	Atomic number of medium	Si: 14
ze	Charge of incident particle	
$\delta(\beta\gamma)$	Density effect correction to ionization energy loss	
β	v/c	
γ	Lorentz factor $(1-\beta^2)^{-1/2}$	
T_{max}	Maximum energy transfer per collision $\frac{2m_e c^2\beta^2\gamma^2}{1+2\gamma m_e/M+(m_e/M)^2}$	MeV
I	Mean excitation energy	eV
α	Fine structure constant	1/137.036
L_{rad}	for $Z > 4$: $\ln(184.15 \times Z^{-1/3})$	4.336 (for $Z = 14$)
L'_{rad}	for $Z > 4$: $\ln(1194 \times Z^{-2/3})$	5.326 (for $Z = 14$)
$f(Z)$	Calculated with approximation 3.6	0.0124 (for $Z = 14$)
ρ	Material density	Si: $2.33\,\mathrm{g/cm^3}$

Table 3.1: Summary of the used variables for the Bethe-Bloch (eq. 3.3) and radiation length equation 3.5 with their units respectively values for Si. The values for L_{rad} and L'_{rad} have been taken from *Tsai, Y.-S. (1974). Pair production and bremsstrahlung of charged leptons.* [15] who has calculated and tabulated values for X_0, L_{rad} and L'_{rad}.

path length of a particle traversing through a medium, over which a high-energy electron loses $1/e$ of its energy by bremsstrahlung [14].

$$\frac{1}{X_0} = 4\alpha r_e^2 \frac{N_A}{A} \left\{Z^2[L_{rad} - f(Z)] + ZL'_{rad}\right\} * \rho \tag{3.5}$$

The function $f(Z)$ is an infinite sum, but can be approximated with a good accuracy by this formula [14]:

$$f(Z) = a^2\left[(1+a^2)^{-1} + 0.20206 - 0.0369a^2 + 0.0083a^4 - 0.002a^6\right] \tag{3.6}$$

with $a = \alpha Z$.

With the values of table 3.1 the radiation length (eq. 3.5) for Si becomes,

$$X_0^{Si} = 9.34\,\mathrm{cm} \tag{3.7}$$

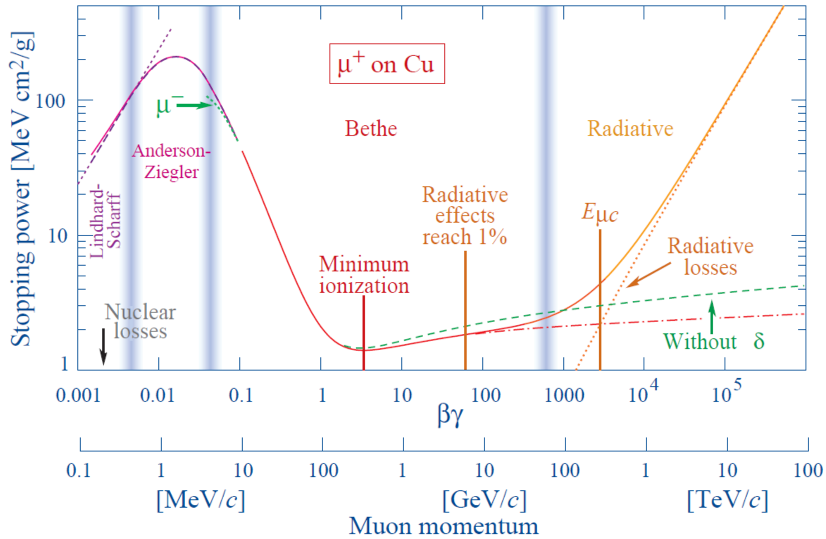

Figure 3.6: The stopping power for positive muons in copper as a function of the particle momentum [14]. The graph shows 4 different approximation regions, separated by vertical lines. The minimum is located around 3 $\beta\gamma$.

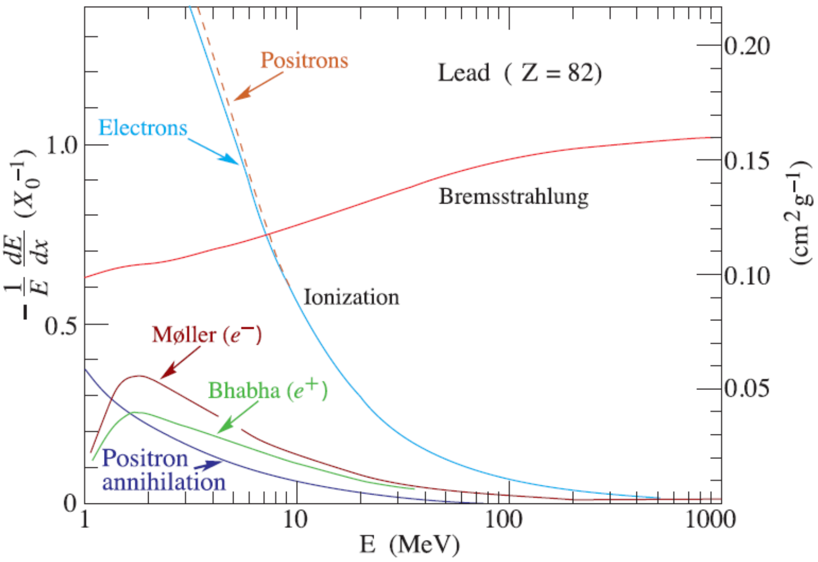

Figure 3.7: This graph shows the fractional energy loss per radiation length in lead as function of electron or positron energy [14]. For lower energys electron (positron) scattering (ionisation, Møller and Bhabha) are the main cause for the high energy loss. For higher energies the contribution of this processes drops logarithmically and bremsstrahlung dominates.

3.1.5 AC-coupling

DC-coupled sensors have the disadvantage of having the p-strips reverse current flowing through the amplifier, which leads to a shift of the operating point. Usually multiple amplifiers, each linked to a single strip, are connected to a multiplexer. The high offset differences between the strips would lead to an dynamic range cut off. Furthermore the high temperature dependency of the reverse current would require a continous offset correction. To avoid these problems, it is commonly agreed that the sensors are AC-coupled. The therefore needed coupling capacitors are integrated in the sensor architecture. They are realized by a $100-200\,\mathrm{nm}$ thick SiO_2 layer between the strip implant and the aluminum strip on the surface. Due to the fact, that the value of C_C dependends on the strip geometry, it is usually given in geometric indepentend units, usually $\frac{\mathrm{pF}}{\mathrm{cm}\,\mathrm{\mu m}}$.

3.1.6 Bias resistor

As described earlier the sensor must be depleted by applying a depletion voltage V_{dep}. Because it is not possible to apply V_{dep} to each strip separately, it is connected to the innermost ring, called *bias ring*. The connection between the strip implants and the *bias ring* is established by a high-ohmic *bias resistor*. The *bias resistor* has usually a order of M Ω, and consists of poly-crystalline silicon. The resistivity depends on the length of the poly-crystalline structure. So to avoid a waste of space for large resistors, the poly-crystalline silicon is shaped like meanders (fig. 3.8). Although there are other methods for strip biasing like the "punch-through" methode, the "poly-silicon" methode was preferred for its superior radiation hardness.

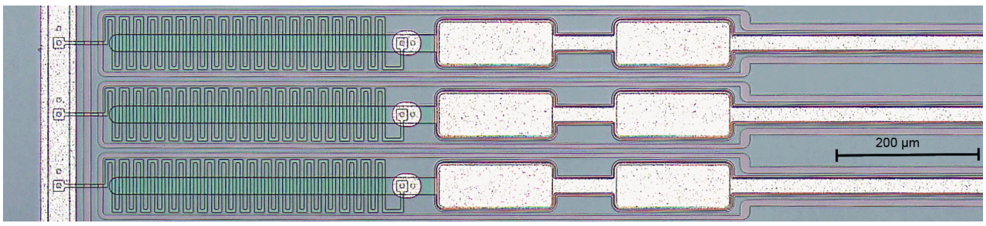

Figure 3.8: The bias ring on the left side is connected to the *strip implant* by the meander shaped bias resistor.

3.1.7 The accumulation/inversion layer

The surface passivation of our sensors is realized by a layer of silicon dioxide (SiO_2). There are many different ways to grow an SiO_2 layer on a wafer, but it can also arise naturally via thermal oxidation (native oxide). The surface conditions of the Si wafer have an important impact on the resulting oxide film. Defects on the Si surface can cause the formation of traps in the SiO_2 layer [16]. Those traps capture positive charges (holes), which in turn attract electrons to the surface, building a conductive layer shortening all n-type doped areas (fig. 3.9). For p-type bulk material this electron layer is called inversion layer and for n-type bulk material accumulation layer.

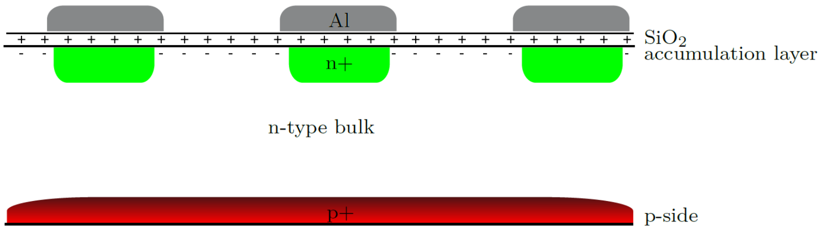

Figure 3.9: The formation of an accumulation layer: Fixed positive charges captured in traps of the SiO_2 layer, attract alectrons to the surface. [13]

In this work two different techniques have been tested to interrupt the accumulation layer: The p-stop and the p-spray blocking methode. The p-stop methode uses additional p-type doped areas, implanted between the n-type strips (see figure 3.10). The p-stop barrier in contact with the n-bulk behaves like a usual p-n-junction, generating a space charge region surrounding the p-stop area. This region is free of charge carriers and repels all electrons interrupting the accumulation layer.

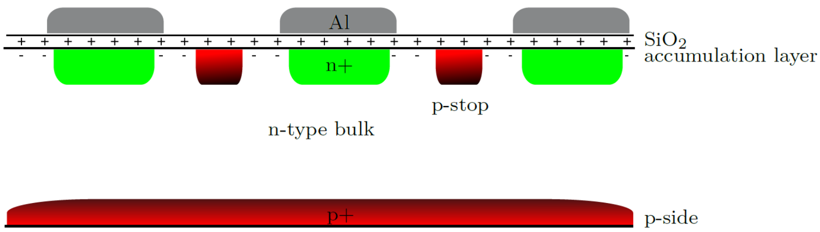

Figure 3.10: Interrupting the accumulation layer with an additional p-type doped area, called p-stop. [13]

The p-spray methode uses a simpler approach to isolate the n-type strips by converting the bulk near the surface from n to p-type. This is done by implanting acceptors over the whole sensor surface (see figure 3.11). The acceptors compensate with the accumulated electrons, removing the accumulation layer completely. This methode only works if the dose and energy of the implanted ions is chosen properly, to avoid an overflow or lack of acceptors.

The n-strips of the p-spray sensor, used for the experimental series in chapter 5, should be completely embedded in p-type material. Therefore the implantation energy was much higher than for the p-stop sensors to achieve a deeper doping profile of the p-type area. Also the doping concentration was reduced drastically.

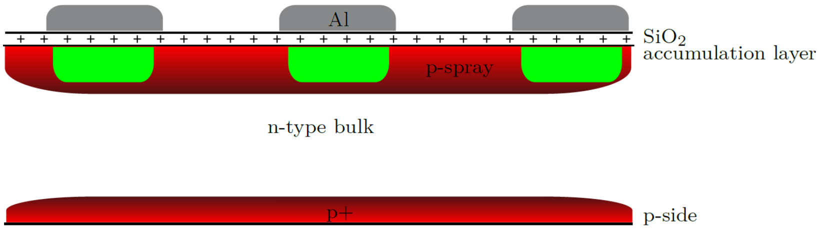

Figure 3.11: Interrupting the accumulation layer with the p-spray approach. [13]

3.1.8 Other sources of e-h-pairs

Sources of e-h-pairs are beside charged particles, also thermal and electromagnetic excitation. Thermal excitation is the heat energy transfer from the environment to an electron. The possible amount of transfered energy E_{Therm} is proportional to the temperature with the Boltzmann constant as proportional factor:

$$E_{Therm} = k_B T \tag{3.8}$$

Even if E_{Therm} is smaller than the energy needed to overcome the energy barrier, defects in the crystal lattice can make an e-h-pair creation possible. Hence, at room temperature the actual sensor signal is overlayed with a thermal noise.

Electromagnetic excitation is the absorption of a photon and can also be a reason for the generation of a new e-h-pair. The transfered energy depends on the photons wavelength and must be higher than the energy barrier (ΔE) between the valence and conduction band, to liberate the e^-.

3.1.9 Equivalent Noise Charge (ENC)

The information about sensor noises in this subsection was taken from the PhD thesis of Manfred Valentan [13].

Even if no particle is traversing the sensor, a small stochastic fluctuating signal is detected by the readout electronics. This unwanted signal or noise is the composite result of multiple noise sources and can be described by the "equivalent noise charge" (ENC). As can be seen in eq. 3.9 the overall noise is the sum of four terms. The origin of each term is sketched in fig. 3.12 showing a simplified equivalent circuit diagram of a silicon sensor, seen by the readout electronics. ENC is usually given in number of electrons.

$$ENC^2 = ENC_C^2 + ENC_I^2 + ENC_{R_P}^2 + ENC_{R_S}^2 \tag{3.9}$$

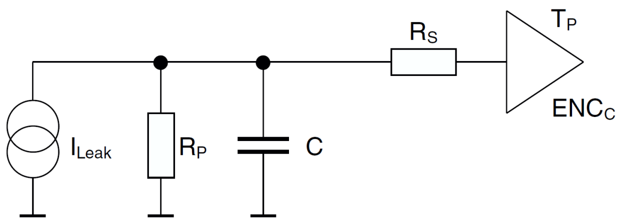

Figure 3.12: Equivalent circuit diagram of a silicon sensor. [17]

Dark current noise ENC_I: The dark current is one of the main noise sources.

$$ENC_I = \frac{\mathrm{e}}{2}\sqrt{\frac{t_{int} I}{q_\mathrm{e}}} \approx 107\sqrt{t_{int} I}, \tag{3.10}$$

with e ≈ 2.71828 as Euler's number, q_e the elementary charge in Coloumb, t_{int} the integration time of the readout chip in µs and I as the dark current in nA.

Parallel resistor noise ENC_{R_P}: The thermal generated noise contribution of the parallel resistor can be described by,

$$ENC_{R_P} = \frac{\mathrm{e}}{q_\mathrm{e}}\sqrt{\frac{k_\mathrm{B} T t_{int}}{2R_P}} \approx 772\sqrt{\frac{t_{int}}{R_P}} \tag{3.11}$$

As can be seen, a high parallel resistor reduces the noise. Thats why it is always tried to maximize the bias resistor.

Serial resistor noise ENC_{R_S}: The aluminum strip above the implant has also a thermal noise contribution, which shows up as an serial resistor in the equivalent circuit.

$$ENC_{R_S} = \frac{\mathrm{e}C}{q_\mathrm{e}}\sqrt{\frac{k_\mathrm{B}TR_S}{6t_{int}}} \approx 0.395C\sqrt{\frac{R_S}{t_{int}}}, \tag{3.12}$$

Note, in contrast to ENC_{R_P} and ENC_{R_S}, lowering the integration time t_{int} would increase the noise.

Capacitive load noise ENC_C: The sensor capacitance seen by the input of the amplifier channel, has also an impact on the noise level and can be estimated by this simple formula:

$$ENC_C = a + b \cdot C \quad \text{with} \quad C \approx C_{int} + C_{back} \tag{3.13}$$

a and b are given by the amplifier design and can be considered as constant. C is the sensor capacitance and can be approximated by the sum of the interstrip capacitance C_{int} and the backplane capacitance C_{back}. However, a reduction of ENC_C is only possible, by minimizing the sensor capacitance, for example by shortening the strip length.

More detailed information about the interstrip capacitance, can be found in chapter 5.

A very important parameter for the quality of a sensor is the so called signal-to-noise ratio (SNR). It is defined as the ratio of signal S to noise ENC.

$$SNR = \frac{S}{ENC} \tag{3.14}$$

4 Database

As described in the previous chapter the new Belle II detector will consist of 49 ladders with a total of 187 sensors. The necessity to keep track of each sensor and its status has led to the idea of creating a specialized database. The database should store all the information about the sensors and provide an easy access to the measurement data. Other important features of the system are user management with permission handling, a history for each item and the possibility to manage item transfers from one location to another.

In general an item could be a composition of different components, which are itself items. For example, a ladder is made out of a couple of modules and each module contains among one sensor lots of other parts. It is laborious to store all kind of items (sensors, wafers, ladders etc.) with a relational scheme. The reason is that a relational database management system (RDMS) stores the data within tables. The information about an item gets stored in a row of the "items"-table with a unique number, this set of data stored in a row is called a tuple. To describe a relation between an item with its component, one has to create another table where the unique ids of both items are combined to a tuple. The problem is querying the related components of an item, because the only way to do this is by joining this two tables, which can be very complex and time consuming, especially for larger tables.

To get rid of this weakness it was considered to create a object-oriented database management system (OODBMS) instead of an conventional RDMS. While a relational database saves all information of an object in tables, a OODMS offers the opportunity to store the data encapsulated in an object. This approach benefits enormous when querying information, because the database only has to read the component ids within the object of the composite item and search for them. Those search algorithms can be implemented very efficient and fast. There is no need of joining large tables. The drawback of OODBMS is the relative rare use in companies, so that many important tools do not support this kind of database management system and in some cases the performance can also drop significantly which can destroy all performance benefits of an object based scheme.

So to keep the administrative effort minimal for this project a RDMS was taken, because the database server for the application was already running a very reliable RDMS. The loss of performance caused by joining tables could be minimized by developing a good database model and by optimizing the use of joins.

An additional request was to implement the whole user interface as a web service. So that everybody can access the database within a simple browser and without the need of installing a client software. Due to security reasons, support and a well documented library for interacting with SQL-databases, a php-framework was chosen. There is a wide range of very different frameworks, but after some testing the choice fell on the cakephp framework [1] . It is an open source project developed by a non-profit organization, the Cake Software Foundation [2]. The main reasons which lead to this decision were: it has a very large community, it is licensed under the MIT license[18] and it uses a very nice approach called "convention over configuration". Convention over configuration means that by following simple rules, like naming conventions of database tables and their columns, the framework is able to generate lots of functionality automatically. The developer can so minimize the effort of writing configuration files.

Another difficult problem was the saving of measurements in a flexible and efficient way. There is a huge variety of measurements, and each one is collecting a different set of data. They differ in amount of collected data as well as in number of parameters saved for each measuring point. Furthermore for some measurements it is important to save the start and the stop time and other parameters, which never change during the process, so they should only be saved once per measurement and not for every measuring point to reduce redundancy. Also the system should be capable of saving measurements, which are not yet in the setup but could be interesting in future. So the aim was to implement a system which was as general as possible.

There are three tables to save all measurement data called `measurements`, `measuring_points` and `readings`. Each measurement has lots of measuring points and each point can have any number of related readings. Readings are storing one value and its assigned parameter.

[1] Cakephp Framework, website `http://cakephp.org/`
[2] Cake Software Foundation, Inc. website `http://cakefoundation.org/`

4.1 Database model

The whole database consists of over 40 tables. For a better overview the tables are categorized into three layers. Each layer represents one of the main database functionalities:

- Administration
- Logistics
- Measurement data

Figure 4.1 shows a simplified Entity-Relationship-Model of the database. Only showing the most important tables and relations.

4.1.1 Administration

The administration layer provides the functionality for the user management. It contains all tables, which are holding user data and their permissions.

The permissions are set with access control lists (ACLs). The ACL tells if an "access request object" (ARO) is allowed to access an "access control object" (ACO). In our case an ARO is a user or a group and the ACOs are the functionalites of the database.

The administration layer is also responsible for logging all critical user actions, like deleting an item, which are saved in the `logs` table.

4.1.2 Logistics

The responsibility of this layer is to keep track of each item and to store each work step performed on it in an history.

The logistic functionality was the main reason for this database, therefor it is the biggest and also most important one. Of course the `items` table plays a key role here. In this table each sensor, wafer and all the other important components of a detector are stored with an unique id and an unique code. The id is an auto incremented numeric value, which is often used in the database as a foreign key for lots of relations. The code can be anything a number, name or a combination of both, but it has to be unique. This code gets printed and sticked as an 2D QR-code on each item so it can be identified with a simple scan of this code within the database.

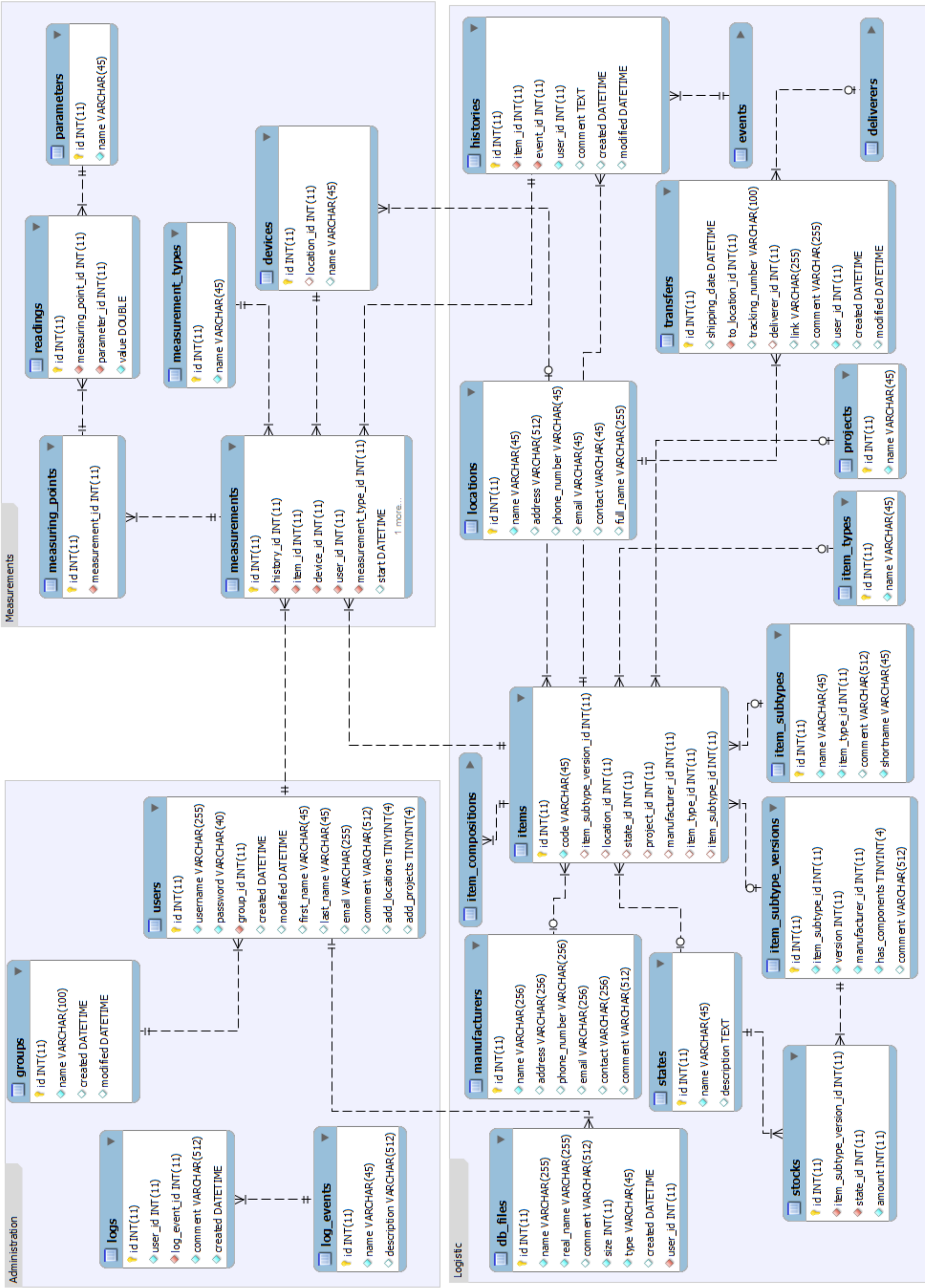

Figure 4.1: Simplified Entity-Relationship-Model with the most important tables and relations.

Types, Subtypes, Versions The construction and development of an detector needs lots of different kind of sensors, chips, modules, test-structures and so on. To get a system into this unmanageable number of item types there are three tables:

- `item_types`
- `item_subtypes`
- `item_subtype_versions`

The `item_types` table holds all the superior types like wafer, sensor, module or test-structure. The subtype delivers information about which kind of sensor or wafer the item is. There are also different versions of the same type, because during the development process each component gets enhanced and for each enhancement a new version is necessary to map this progress to the DBMS.

Annotation The `items` table has a redundance saving the `item_type_id`, and the `item_subtype_id`, because both could be figured out with the `item_subtype_version_id`. But this would be very inconvenient for many items. So in this case, a small redundance was accepted for a better performance.

States For the project management it is necessary to get a quick overview about how many sensors are tested and working within limits. For this reason the state field was implemented, it offers the opportunity to search for items, classified with five stars (*****), which means they are tested and work very well. Items rated with only one star (*) may work but it is not a good idea to use them for the final detector. It is possible to add more verbose states to the system like destroyed or disassembled.

Transfers The Belle II project is a collaboration of many institutes. Often an item gets transferred from one institute to another for testing, assembling or some other reasons. All this transfers are recorded in `transfers`. Beside the item ids of each item transferred, also the responsible delivery service the shipping date and other additional informations are saved.

4.1.3 Measurement data

The third layer of the system manages the measurement data. The idea was to create a platform where all measurement results for every item can be uploaded and viewed. The difficulty was to create a concept that supports all kinds of measurements. The simple approach of creating a table for every kind of measurement would not only result in an unmanageable amount of tables, it would also be very inflexible and make it almost impossible to integrate new measurement types to the system.

The solution to achieve high flexibility by eliminating the effort of managing dozens of different measurement tables, was to store every measurement in a virtual table. How this is done will be explained later by an example. But first it is important to get an overview of the tables and the data they store. With the virtual table concept it is possible to store every kind of measurement within eight tables.

- measurements
  * id
  * history_id
  * item_id
  * device_id
  * user_id
  * measurement_type_id
- measuring_points
  * id
  * measurement_id
- readings
  * id
  * measuring_point_id
  * parameter_id
  * value
- measurement_types
  * id
  * name
- parameters
  * id
  * name
- devices
  * id
  * location_id
  * name
- measurement_sets
  * id
  * name
  * comment
- measurements_measurement_sets
  * id
  * measurement_id
  * measurement_set_id

The table `measurements` relates the measurement data to the measured item, the corresponding history entry of this item, the measurement device, the responsible user operating the measurement and to the type of measurement. Each measurement represents a collection of measuring points. Each measuring point is related to a bunch of readings, which are holding the real values of the measurement for one parameter.

Some quality tests are a set of multiple measurements these sets are saved in `measurement_sets`. The relation `measurements_measurement_sets` links the set with the single measurements.

Figure 4.2 shows an example of how a set of two measurements will be saved. In the example below each measurement produced an output file. The user uploads these files to the server where they will be parsed. The database creates now for each measurement an entry in the `measurements` table with an unique id. This id is used as an foreign key in the `measuring_points` table, to relate each point to one measurement. These measuring points have also a unique id so that each reading can be assigned to the correct point.

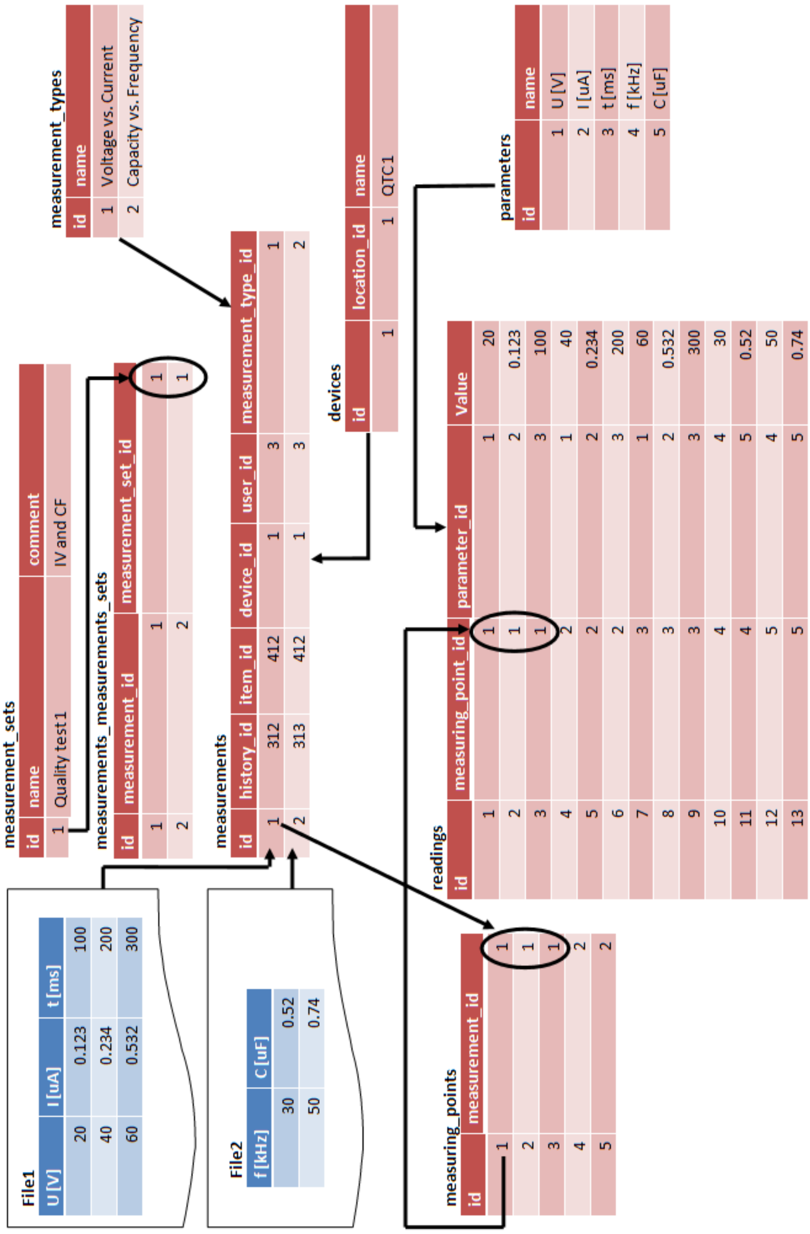

Figure 4.2: An example of saving a set of two measurements in the database.

4.2 User interface

4.2.1 The inventory and detailed item view

The web interface is available under `http://hephy.at/hephydb`. After the login screen the user is shown a statistic about the current amount of saved items categorized by project, status and location. It is possible to adjust the statistic by setting filters for specific item types, manufacturers or other criteria. The menu to set those filters is by default hidden, to open it a click on "Extended search..." below the item code field is required. Screenshot 4.3 shows the statistic page with the open filter element.

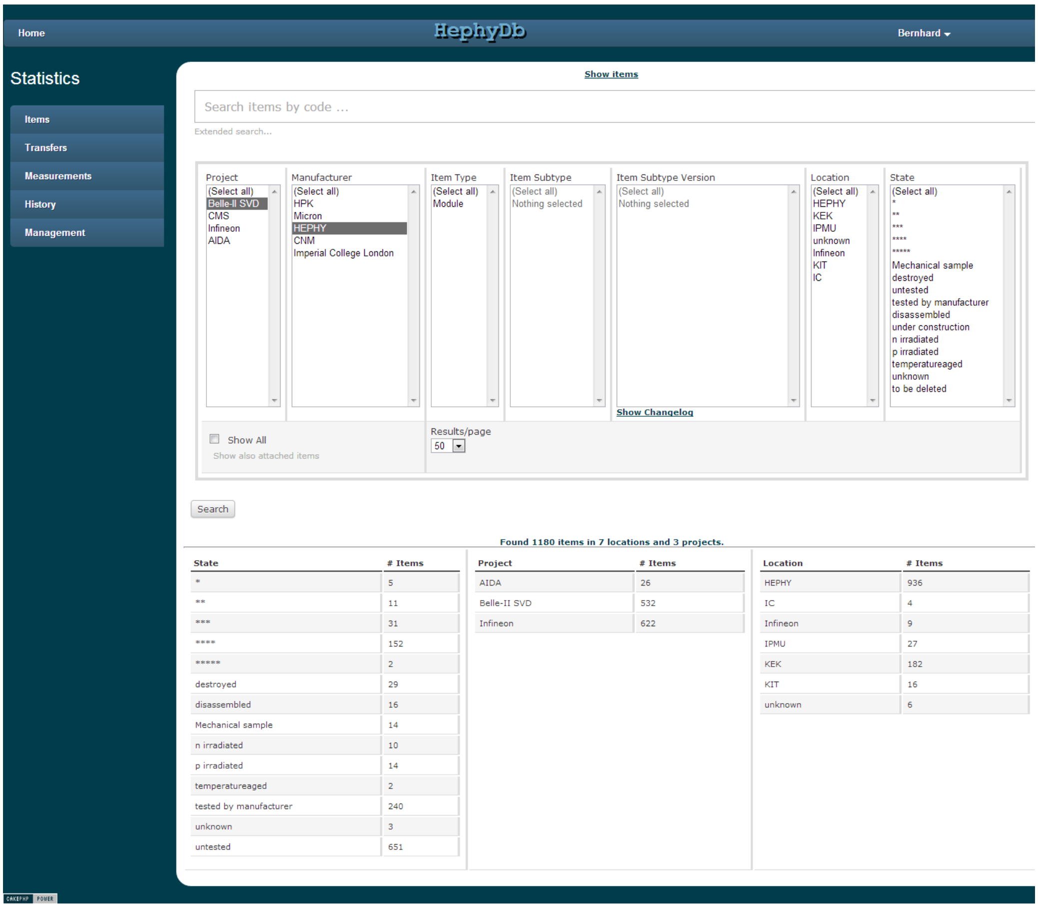

Figure 4.3: Screenshot of the item statistic, represented after logging into the HephyDB.

With a click on "Show items", in the upper region of the statistics page, one can switch to the inventory (fig. 4.4). The inventory offers an overview and shows some basic information about single items. Like the statistics view it is also possible to set filters and search for specific items by entering an item code.

Clicking on an item code forwards the user to the item page (fig. 4.5). Here the user can view detailed information about the item, its history, measurements and transfers. Furthermore it is possible to view or upload related files to this item, add a comment or transfer it to a other location.

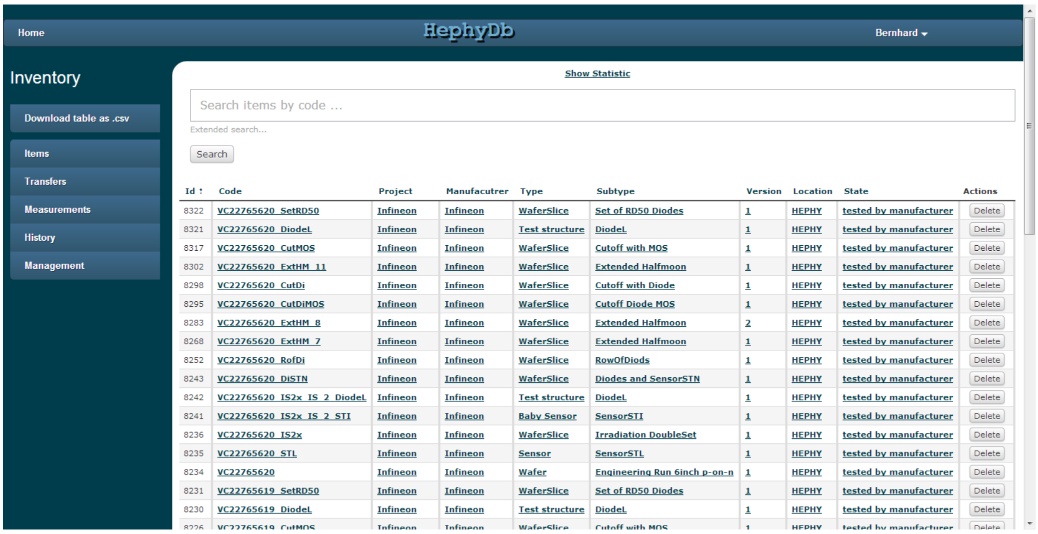

Figure 4.4: Screenshot of the inventory view.

Figure 4.5: Detail page of an item.

4.2.2 The workflow of registrating a new item

Before adding a new item the manufacturer of the item must have been created and added to the project. Also the necessary *Item Type*, *Subtype* and *Subtype versions*. Only then it is possible to register or assemble a new item.

For a better understanding the procedure of creating a completely new item with all its *Item Types*, *Subtypes*, *Subtype versions* and *Components* is explained based on an example:

Lets think of a wafer. The wafer has in the middle one rectangular main sensor and many teststructures on the edges (fig. 4.6). Usually a wafer gets cut into pieces. In our example the manufacturer delivers the wafer cutted into four parts. The biggest one is the main sensor and the other three are the edges of the wafer with all the teststructures. Because of their shape they will be referred as "Halfmoons".

The teststructures on each halfmoon are almost the same but they have some

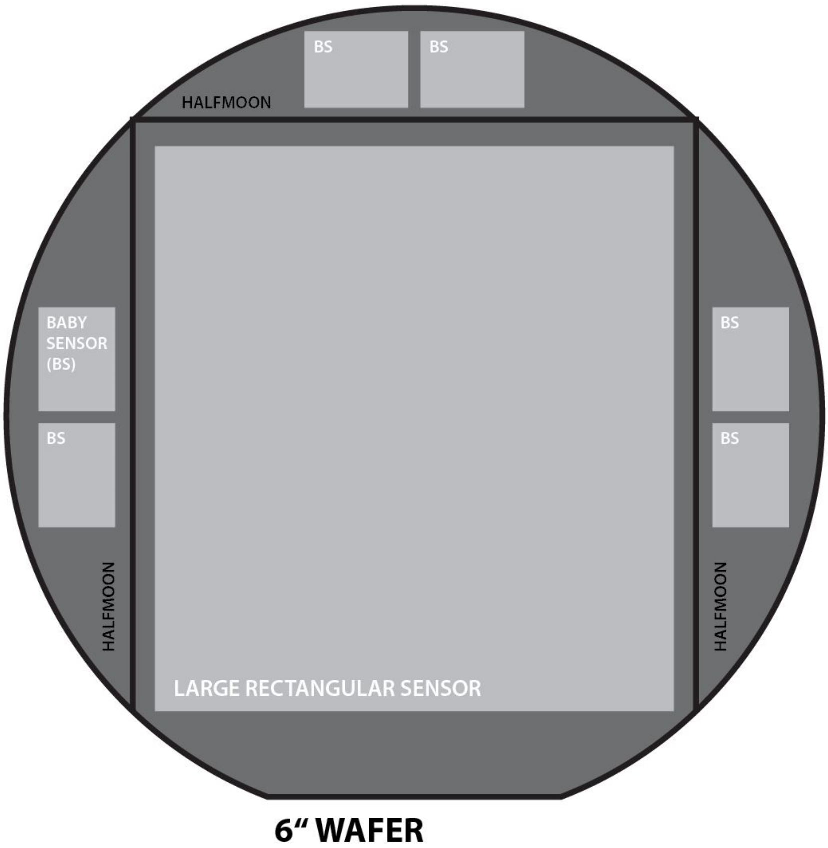

Figure 4.6: Sketch of the wafer layout.

minor changes. So we have different versions of the same teststructure.

First we have to create the manufacturer who produced this item and if present, also all the manufacturers of the components of this item. In our case there is only one manufacturer involved. Creating a new manufacturer is very straight forward. The user only has to select from the Menu on the left *Management => Manufacturers => Create new manufacturer* and fill out the form.

The next step is to create the *Item Types*. In the example above there are four different types to register: "Wafer", "Sensor", "Halfmoon" and "Teststructure". These types can be created by selecting *Management => Item Types => Create new type* and entering the name of the new type.

After creating the *Item Type* it is possible to add the associated *Item Subtypes*. For complex items, it is best to make a list with all subtype names and their abbreviations called shortnames. These shortnames are used for the automatic generation of unique item codes. The subtype name should be more specific than the type name. So to continue the example, a suitable name for the 6 inch p-bulk wafer with a large sensor on it could be "6-inch Large Sensor p" and as shortname "6LSenP".

The teststructures are smaller sensors called baby sensors, so we chose as name "Baby Sensor p" with the shortname "BSenP" with different subtype versions (version 1, 2, 3...). The halfmoons consist of baby sensors, their subtype and shortnames are therefor "Halfmoon Baby Sensor" and "HMBSen". Because there are different versions of baby sensors, there are also different versions of halfmoons, depending upon the version of the baby sensors they consist of.

When creating an item subtype which has components, one has to be careful with the order of creating these subtypes. Before creating the composite item one has to create all the necessary components first. So for the above example it is important to create the "Large Sensor" and "Baby Sensor" before the "Halfmoon" and at last the "Wafer", because it needs all the previous item subtypes as components.

After creating this structure it is very easy to register/assembly new items. Registrating a composite item has the effect that all components of this item will be created, with automatically generated codes, as well. On the other hand, if someone assembles a new item, the components of this item need to be already created and added to the database, so that they can be chosen from the inventory.

5 The measurement of the interstrip capacitance

5.1 Interstrip capacitance

The sensor is a complex network of many capacitances, as shown in figure 5.1. In this work it was assumed that the equivalent circuit of double sided sensor is equal to the single sided, because the strips on the bottom are all on the same potential.

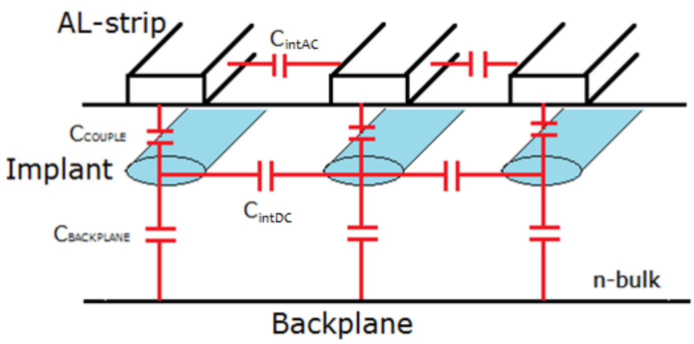

Figure 5.1: Simplified capacity network of a single sided silicon sensor.

C_{int} is a composition of the couple capacitance C_{couple} and the capacities between the neighboring strip implants and aluminum strips, called C_{intDC} and C_{intAC}, respectively.

5.2 Aim of experimental series

For the ohmic side of the DSSD an isolation between the n-doped strips is necessary, to avoid shortcuts caused by the n-bulk basis material. For this reason p-stop barriers are introduced to prevent charge exchange between two neighboring strips. The measurement series performed during this work should reveal the optimal geometry for such a barrier. The aim was to determine the p-stop barrier with the lowest interstrip capacitance. This parameter has an impact on the input capacitance of the readout electronics and therefore influences the signal-to-noise ratio.

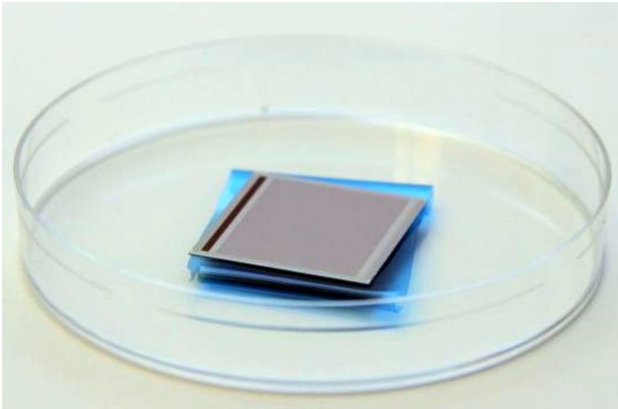

Figure 5.2: Photo of a baby sensor.

5.3 Test sensors

The test sensors have been produced by Micron Semiconductor [1] and are smaller sized than the real SVD sensors. For this reason they are called *baby sensors* with a sensor size of approximately 2.5 cm × 2.5 cm.

There are three basic p-stop geometries: common p-stop, a-toll p-stop and combined p-stop (see table 5.1). Each one was produced in four slightly different versions, varying only in the distance between the p-stop and the n-doped strip implant, shown in figure 5.3). Except of the individual p-stop region, all sensors were identically.

Common	Combined	Atoll	PSpray
	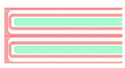	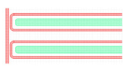	

Table 5.1: The different p-stop geometries. The n-strips are colored green, while the p implanted areas are red.

Additional to these twelve p-stop patterns also a so called p-spray barrier was tested. This barrier differs from the others, because instead of introducing a well defined p-stop geometry, the whole sensor surface is implanted, but with a much lower fluence than the other sensors. Because the whole area between the n-strips is implanted, there is no possibility to create different versions of this kind as we did for the other p-stop patterns. All together thirteen different n-strip isolations have been tested and compared on four different sensors. The combined, common and atoll sensors originated from the same wafer, while the p-spray sensor needed to be manufactured on a second wafer due to its uncommon implant process. All were

[1]Micron Semiconductor Ltd., Inc. website `http://www.micronsemiconductor.co.uk/`

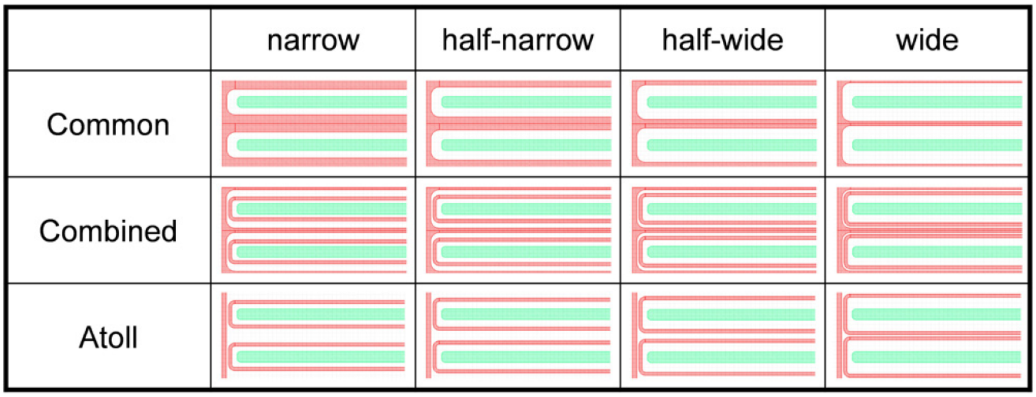

Figure 5.3: Overview of the three basic p-stop geometries and their different versions. [19]

full functional DSSDs, but with much smaller dimensions as the sensors usually used for the SVD. Table 5.2 lists the most important geometrical and electrical sensor parameters.

	narrow	**half-narrow**	**half-wide**	**wide**
Common				
bar width (bw)	40.0	60.0	20.0	10.0
distance (d)	17.5	22.5	27.5	32.5
Combined				
bar width (bw)	10.0	10.0	10.0	10.0
atoll width (aw)	7.5	7.5	7.5	7.5
distance (d)	8.0	12.0	16.0	20.0
Atoll				
atoll width (aw)	7.5	7.5	7.5	7.5
distance (d)	12.5	17.5	22.5	27.5

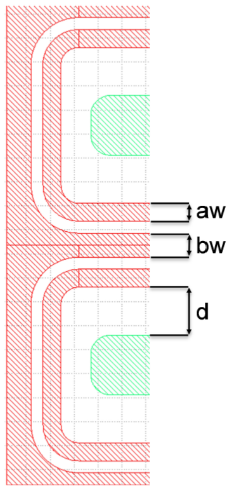

Figure 5.4: The twelve different p-stop geometries. All values in μm. [19]

5.4 Measurement setup

The interstrip capacitance was measured with a HP/Agilent 4285A Precision LCR Meter. The name deflects the capability of this device to measure inductivities L, capacities C and resistors R. This device offers a wide test frequency range from 75 kHz to 30 MHz. As source-measurement unit (SMU) a Keithley 237 was used to apply the bias voltage. The photos in figure 5.5 give an overview of the used

Base material	300 µm n-type silicon, 5 kΩ cm
Full depletion voltage	60 V to 70 V
Leakage current at full depletion	0.43 µA to 0.55 µA
Bias resistance	40 MΩ
Coupling capacitance per strip length and width	$1.13\,\frac{\mathrm{pF}}{\mathrm{cm\,\mu m}}$
Number of strips	256
Pitch	100 µm, no intermediate strips
Strip implant area	2.56 cm × 25 µm
Strip isolation	p-stop, with varying geometry
Strip orientation	perpendicular on p-side and n-side

Table 5.2: Important electrical and geometrical parameters of the tested baby sensors [19].

setup.

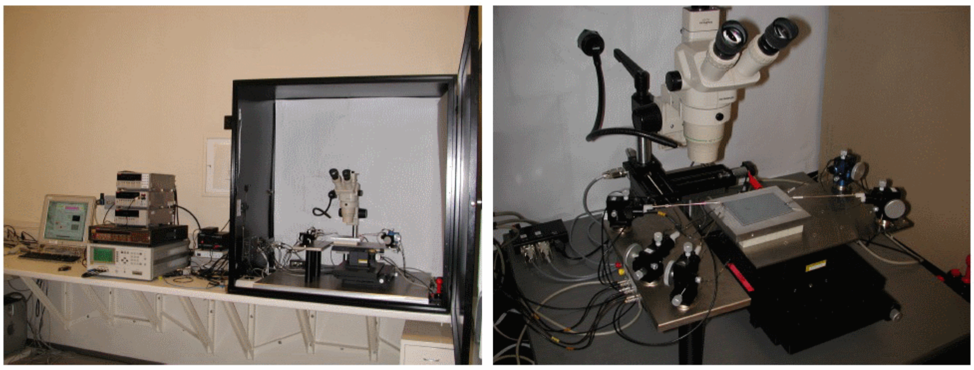

Figure 5.5: A short overview of the used measurement equipment. On the left side: the measurement PC running LabView next to the SMU and LCR meter. On the right side: The inside of the measurement box with the probe needles, the microscope and the vacuum chuck for the fixation of the sensor. [20]

In this work two components of the interstrip capacitance have been determined: the capacitance between the neighboring aluminum strips on the sensor surface, which are connected to so called AC pads and the capacitance between the implanted strips connected to the DC pads of the sensor. In the following these two capacities will be referred as C_{AC} and C_{DC} according to the connection pads used for the measurement. Figure 5.6 shows the circuit diagrams for the C_{intAC} and

C_{intDC} measurement.

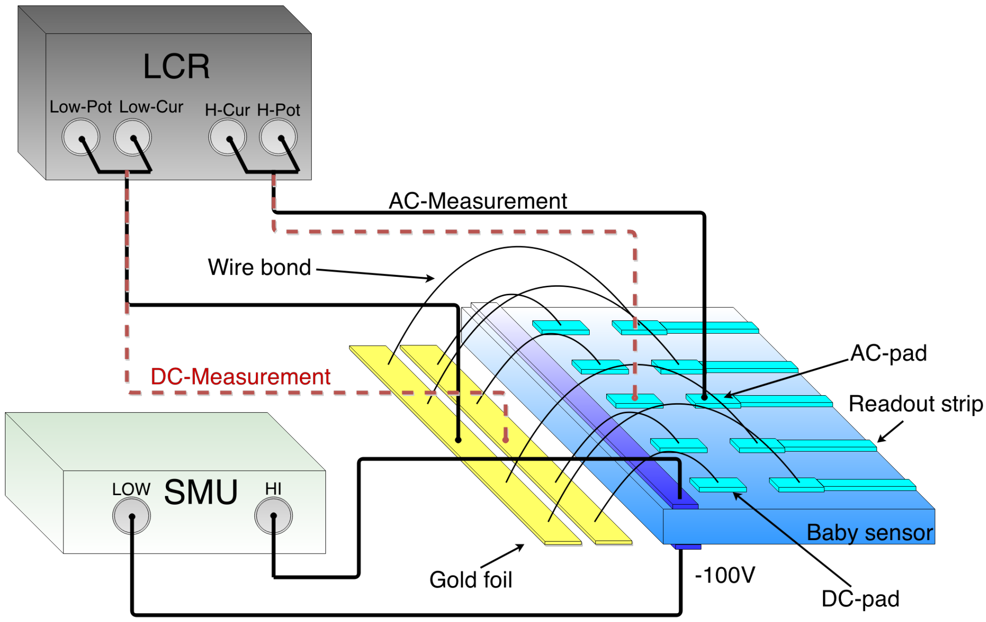

Figure 5.6: A sketch of the measurement setup. As displayed here the n-side is on top and p-side on the bottom of the sensor.

For the measurements the sensors were placed on a vacuum chuck, which was an in-house construction made by the HEPHY workshop. Its integrated probe needle allowed a precise connection of the bias ring on the backplane to the SMU. The other SMU port was connected via a normal probe needle to the bias ring on the n-side. One probe needle, connected to the LCR-meter, was placed directly on the AC/DC pad of the middle strip, while the second one was placed on the gold foil shortening the neighboring AC/DC pads.

During the first attempts for this experiment only one neighbor strip was connected to the LCR meter. After some tests and refinements in the measurement setup, we decided to increase this number to four neighbors, two on each side of the main strip. To include also the impact of the next neighboring strips on the interstrip capacitance. Because of the small distances between the strips, it is very difficult to connect them all with probe needles. For this reason wire bonding was used. The AC and DC pads were not directly shorted, instead the bonds were lead to a gold foil, which was glued onto the carrier plate. Figure 5.7a and 5.7b shows two photos of such bonds taken under the microscope.

As described before, the 256 strips of each baby sensor were divided into 4 regions with slightly different geometric parameters. So each region had 64 strip, subdivided again into 7 groups with 5 strips each (1 test strip and 4 neighbor strips). It was not possible to use all strips for the measurement, due to spacing issues for the bonds some strips were skipped between each group. Also to avoid problems on the edge regions, the outer strips of each region were left untouched. Unfortunately the wire bonding was problematic due to small pad sizes and the relatively long bond length. Nevertheless for each region at least 3 groups could be produced and measured successfully.

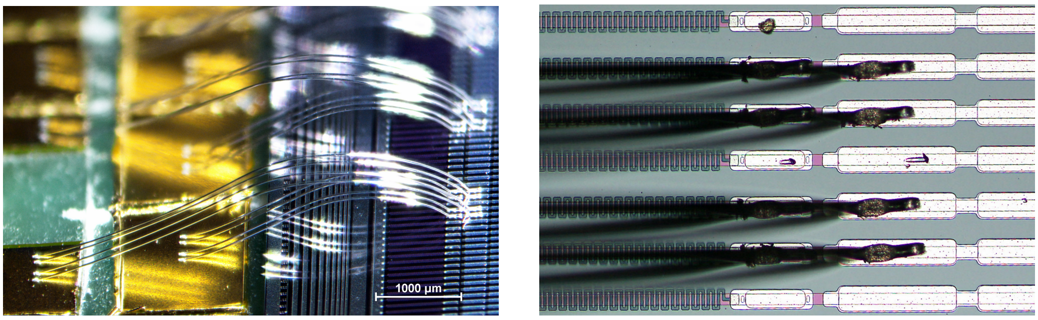

(a) Side view of the wire bonds connecting the neighbour strips to the gold foil.

(b) Topview of the connections between the bonds and the neighbour strip pads on the sensor.

Figure 5.7: Wire bonding of the neighbour strips.

The LCR meter supports three correction functions [21] to suppress parasitic influences:

open Removes the parasitic stray admittance (C, G) of the DUT[1]

short Removes the parasitic impedances (L, R) of the DUT

load Increases measurement accuracy by testing a well defined device and using it as reference.

The short and load correction had only a negligible influence on the measurement results and because their set up was very time consuming, only the open correction was performed before each measurement.

Furthermore the cable correction was activated and set up to $2m$.

The device offers two equivalent circuit modes to measure L, C or R, the serial and parallel mode. The relative impedance magnitude of the reactance, R_s and R_p is crucial for the choice of the best circuit mode.

As recommended in the operation manual of the LCR Meter [21] the parallel circuit mode is best for small capacitances. This arises from the fact that a small capacitance yields a large reactance, so the parallel resistance R_p has more impact on the impedance than R_s (see figure 5.8 (a)). For a large Capacitance the inverse is true and so the preferred mode is serial (see figure 5.8 (b)).

As a thumb rule the operation manual recommends for capacities with an impedance higher than $10\,\mathrm{k\Omega}$ the parallel mode and below $10\,\Omega$ the serial mode. A typical interstrip capacitance has a few pF which corresponds to an impedance of about

[1]DUT ... device under test

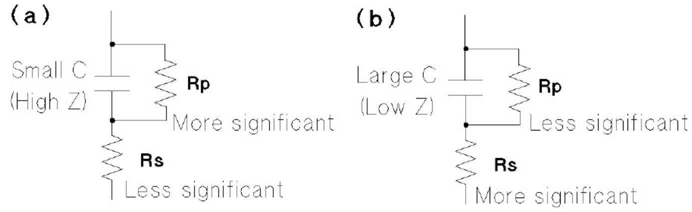

Figure 5.8: Equivalent circuit modes. (a) Parallel (b) Serial [21]

10 kΩ to 100 kΩ at a frequency of 1 MHz. So for all measurements in this work the parallel mode was used.

5.5 Measurement results

5.5.1 C_{AC}

The graph plotted in figure 5.9 shows the measurement results of each p-stop pattern in comparison. Note: For each geometry region (wide, half-wide, half-narrow and narrow) three different strips were measured and plotted. Because they are nearly perfectly congruent over the whole frequency range, it seems that only one curve has been drawn. This also shows up in a very small standard deviation, of $s \approx 0.02\,\text{pF}$ at $f = 1\,\text{MHz}$.

The capacitance measurements on the AC pads showed that on all p-stop patterns the capacitance is indirectly proportional to the distance between the strip and the p-stop barrier. For this reason the "wide" geometries behaved best over the whole frequency range. Interesting is that the p-spray pattern showed also a very low and less frequency dependent capacitance. Noticeable is also the different behaviour of the atoll sensor at lower frequencies ($f < 1\,\text{MHz}$), while the C_{AC} of all the other candidates decreased with lower frequencies the opposite was true for the atoll sensor. But all measurements had in common, that above 10 MHz the capacitance increased rapidly.

5.5.2 C_{DC}

Like the capacitance between the metal strips C_{AC}, the capacitance between the implants C_{DC} decreases with a wider gap between the p-stop region and the strip implant. But for all geometries the capacitance decreases at higher frequencies ($f > 1$MHz). A reason for this behavior could be the decreased implant length contributing to the capacitance for higher frequencies [22]. The strip can be represented as a long chain of low-pass filters. Due to the much higher resistivity of the implant strip compared to the metal strip, the implant suppresses high frequencies stronger. Therefore the active strip length gets shortened.

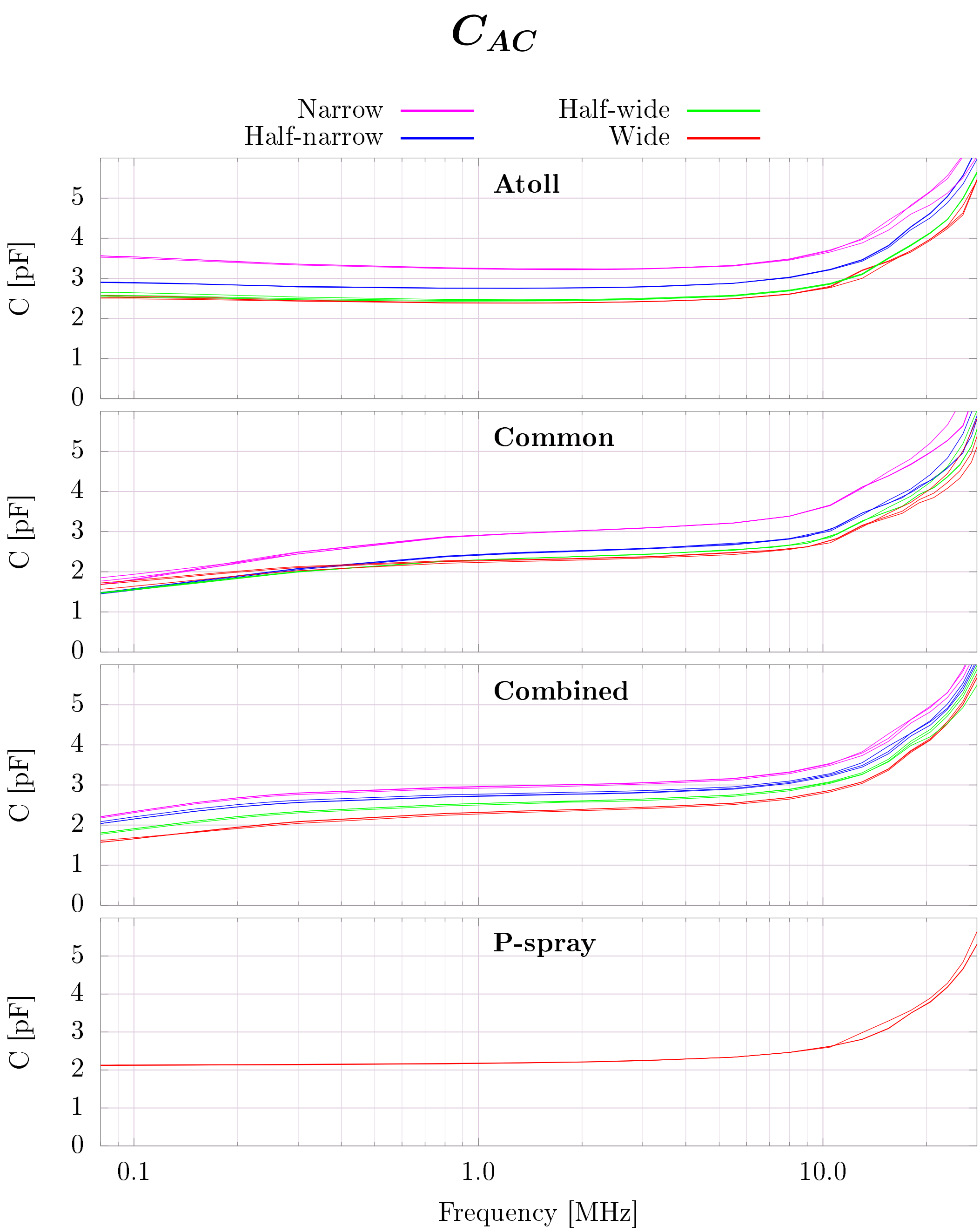

Figure 5.9: The interstrip capacitance between the aluminum strips for the different p-stop patterns.

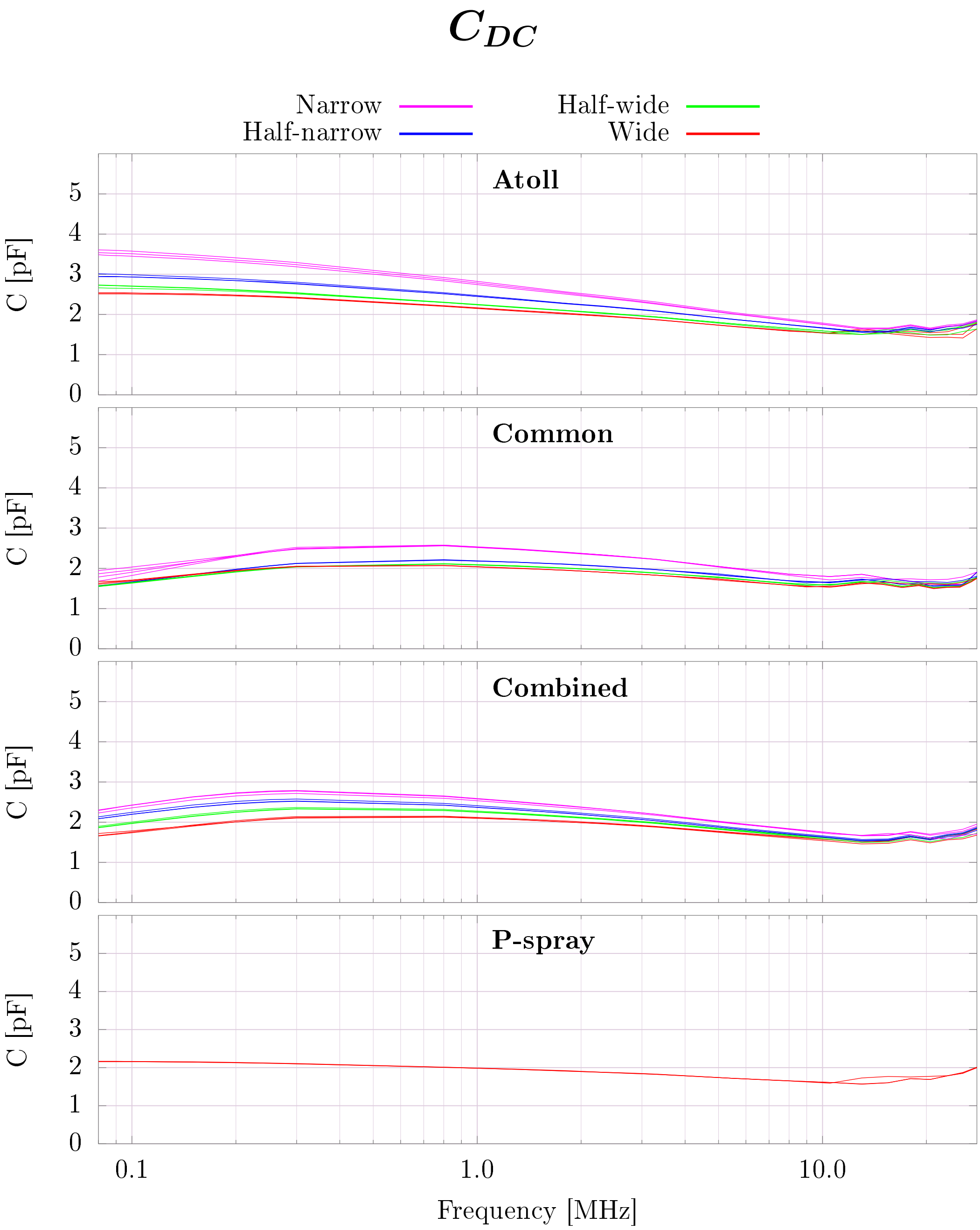

Figure 5.10: The interstrip capacitance between the strip implants for the different p-stop patterns.

5.5.3 Additional measurement results

On the next few pages additional measurement data is shown. R (fig. 5.11 and 5.14) is the parallel resistor of the assumed equivalent circuit (as explained in section 5.4). The used LCR meter was also capable of directly displaying the complex impedance Z (fig. 5.13 and 5.16) and phase shift φ (fig. 5.12 and 5.15). It will be shown in section 6.1.2 that it is possible to convert the values of Z and φ into R and C. So Z and φ are to some extent equivalent to the representation of R and C.

Similar to the previously shown C measurements the impact of the distance variation between strip and p-stop can easily be spotted. As can be seen in figure 5.13 and 5.16 for higher frequencies Z for both the AC and DC measurement is approaching zero for all types displayed. Whereas the phase increases slightly until approximately 10 MHz where it starts to rise stronger. For the φ_{AC} measurement shown in figure 5.12 this effect can be seen very clearly. The origin of this behavior could not be clarified.

The discontinuities of the R measurements, especially for the *common* and *combined* type, are arising because at this frequencies the phase reaches $-90°$, which corresponds to a pure capacitive load.

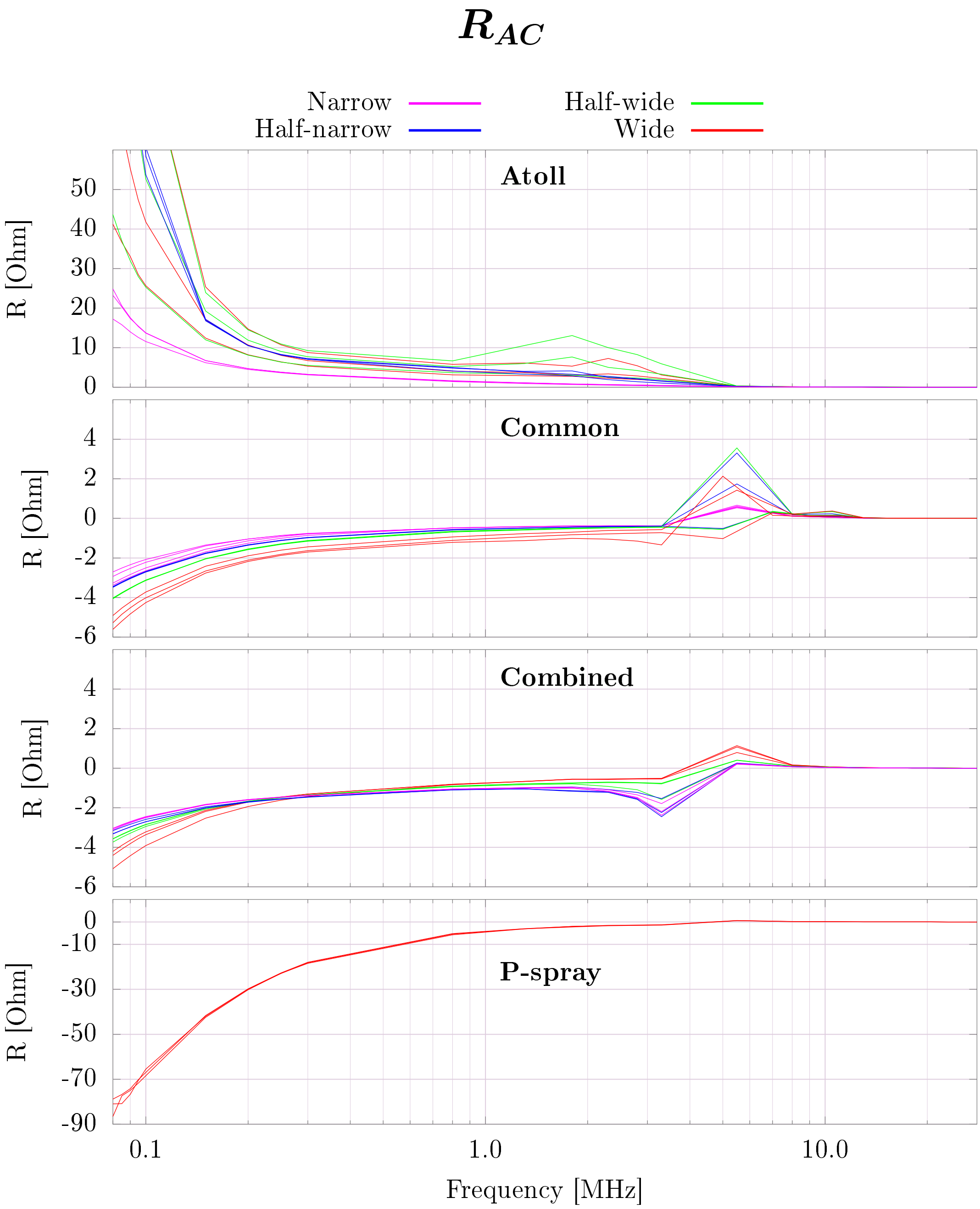

Figure 5.11: The parallel resistance of the C_{AC} measurement.

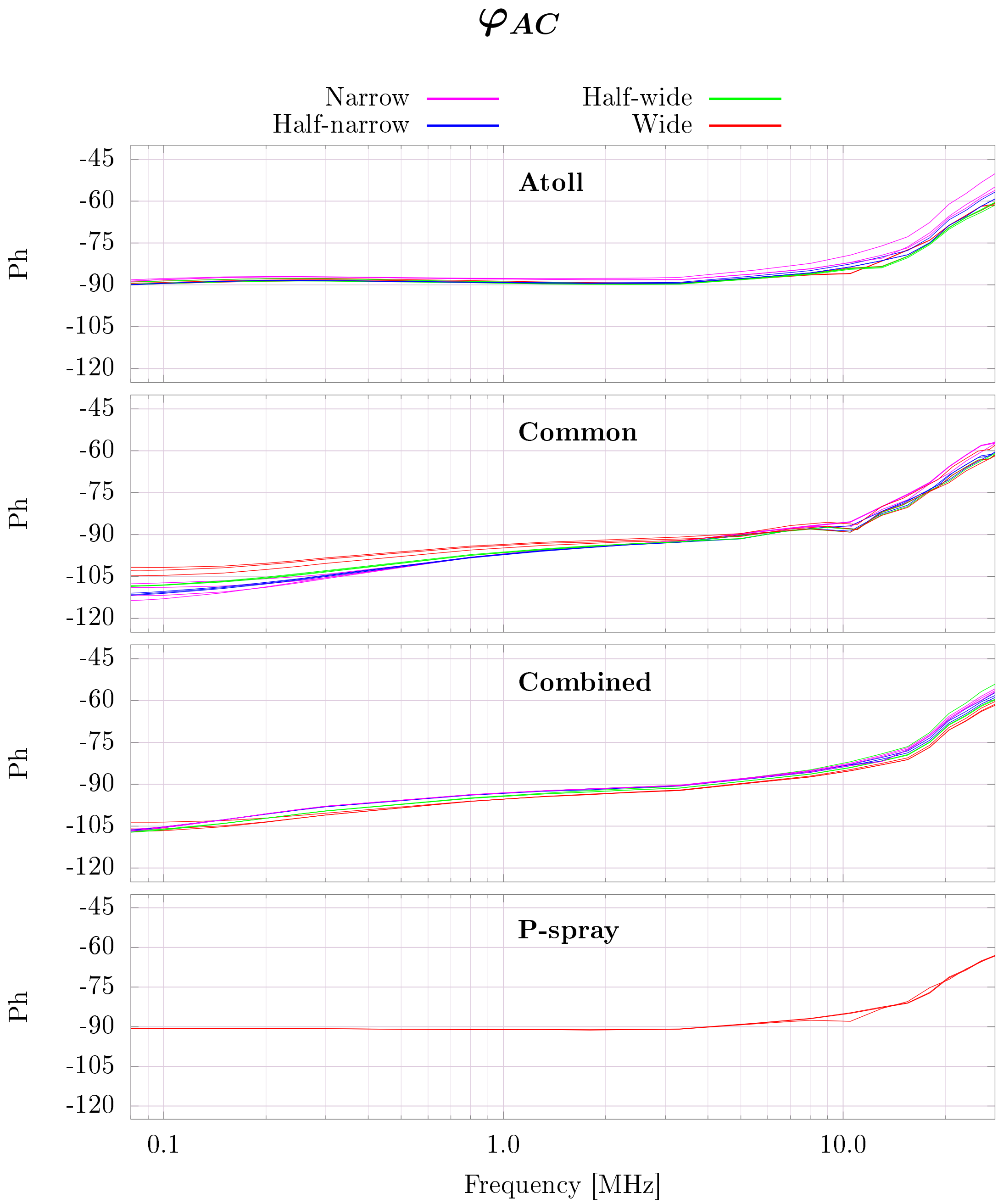

Figure 5.12: The phase shift of the C_{AC} measurement.

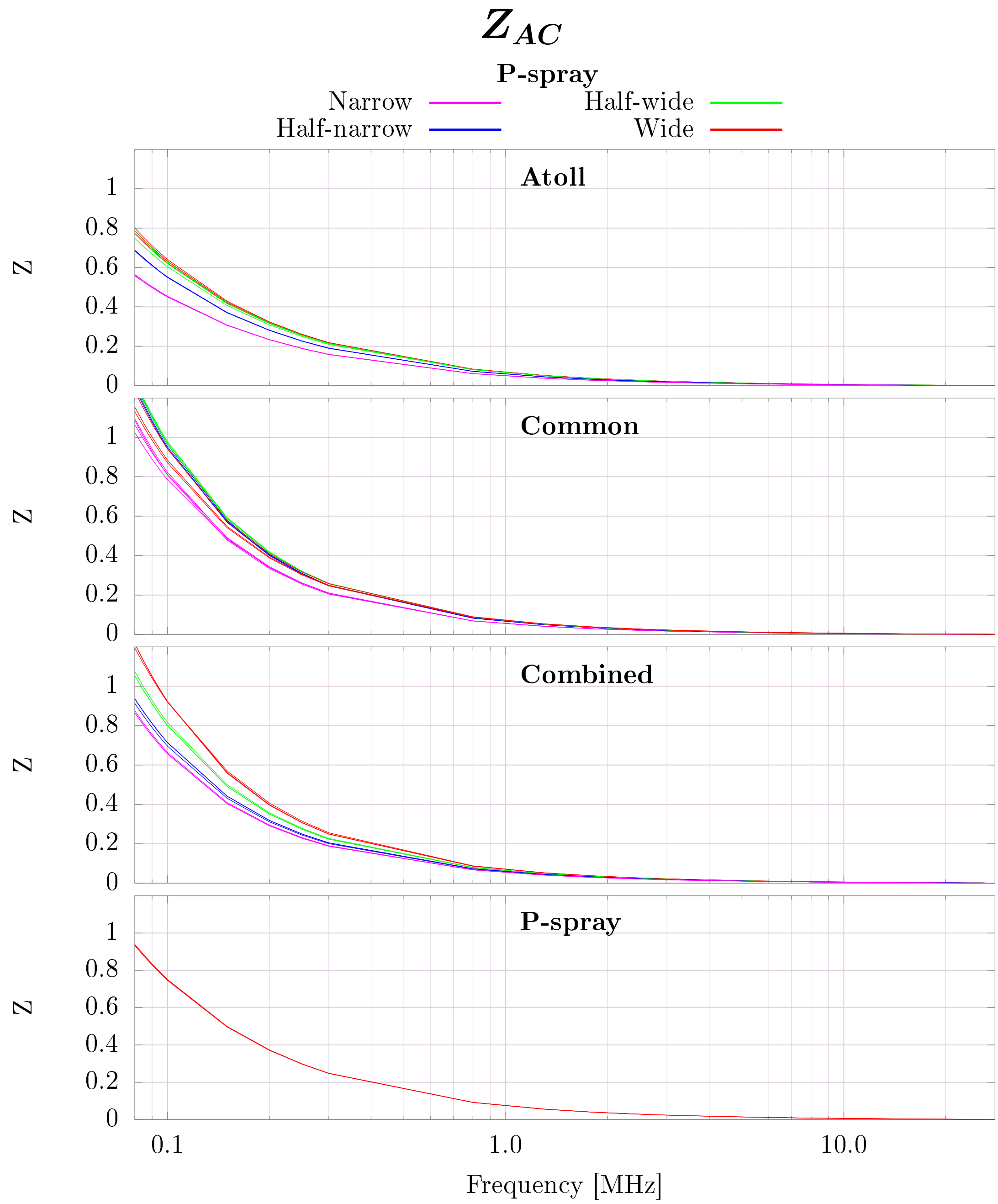

Figure 5.13: The complex impedance of the C_{AC} measurement.

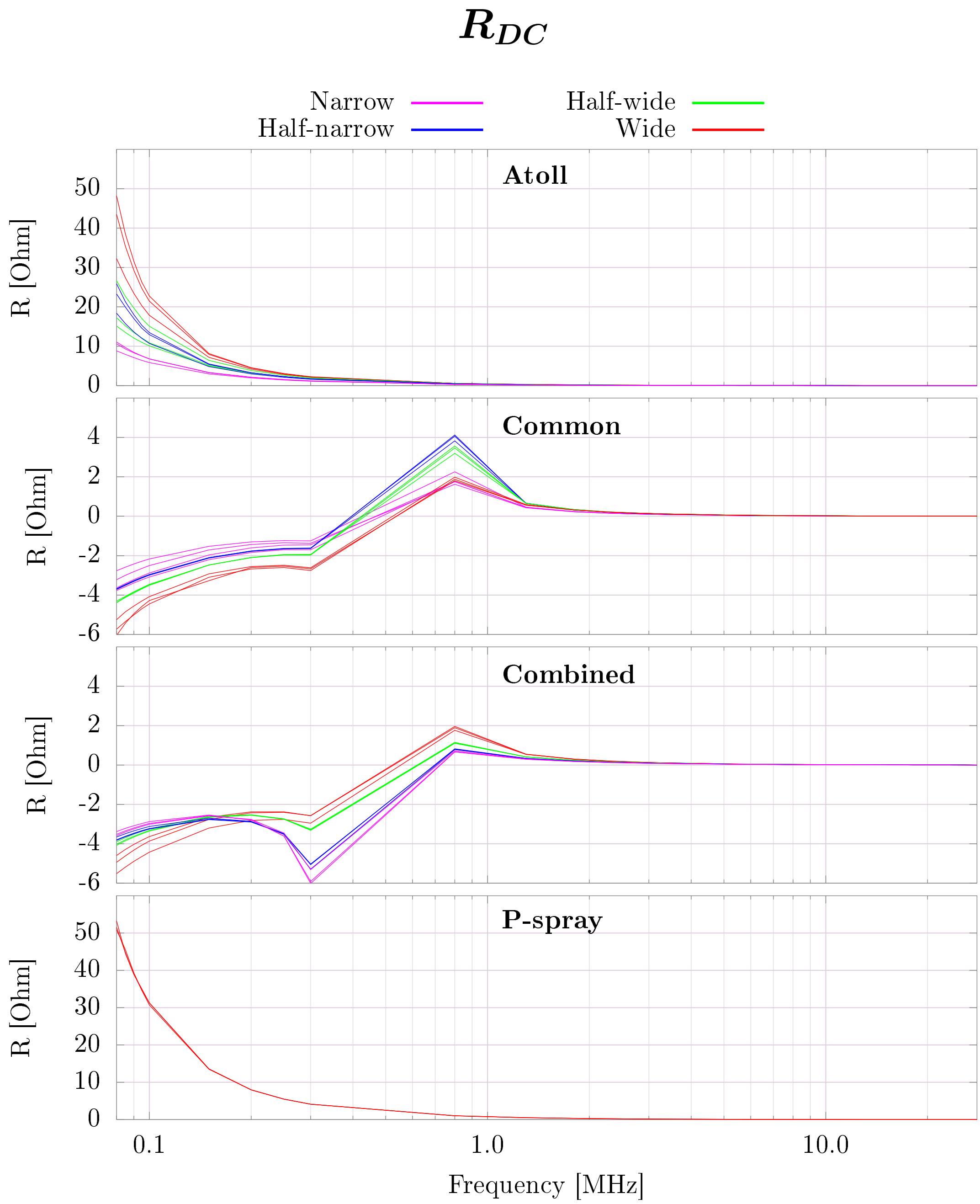

Figure 5.14: The parallel resistance of the C_{DC} measurement.

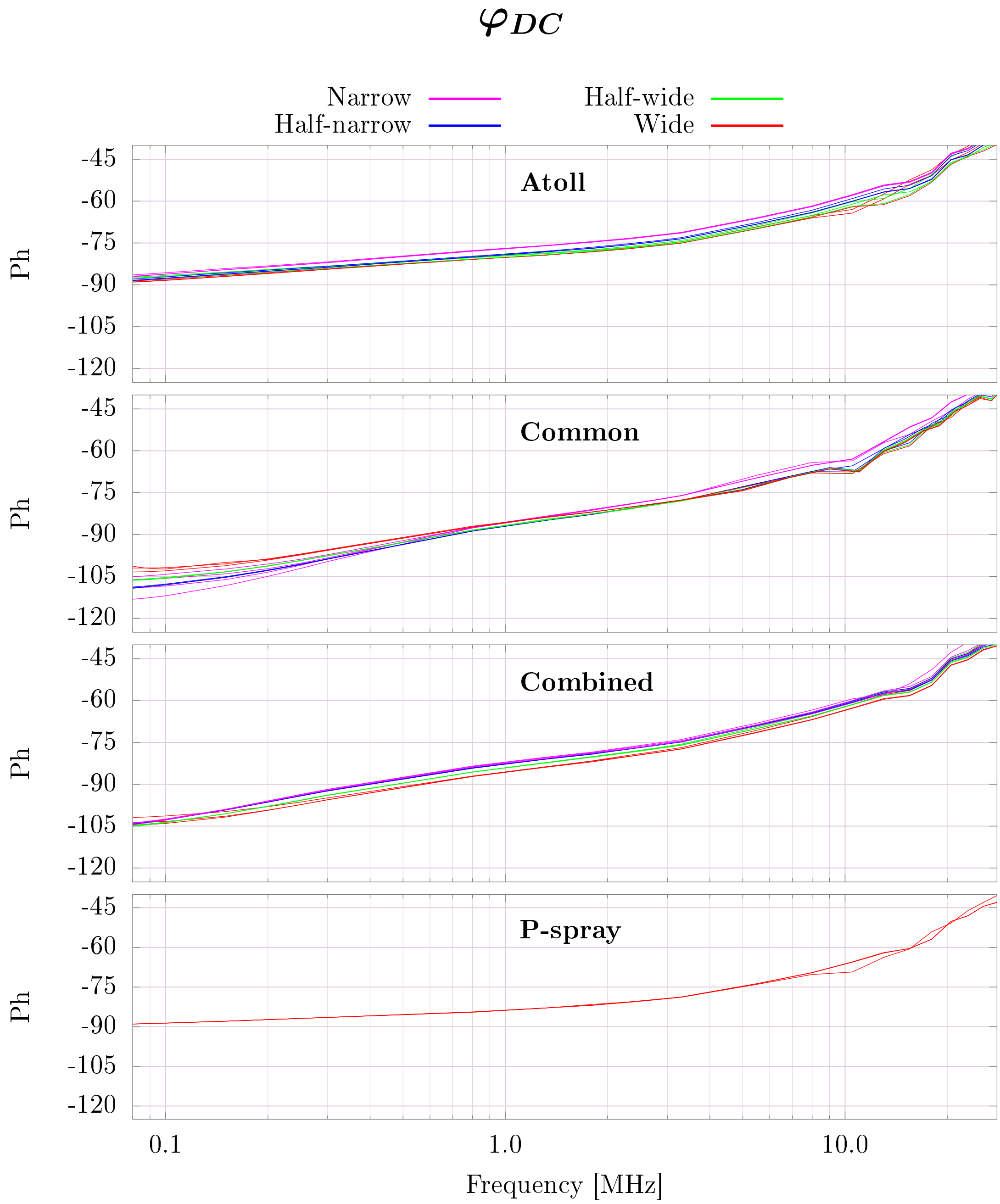

Figure 5.15: The phase shift of the C_{DC} measurement.

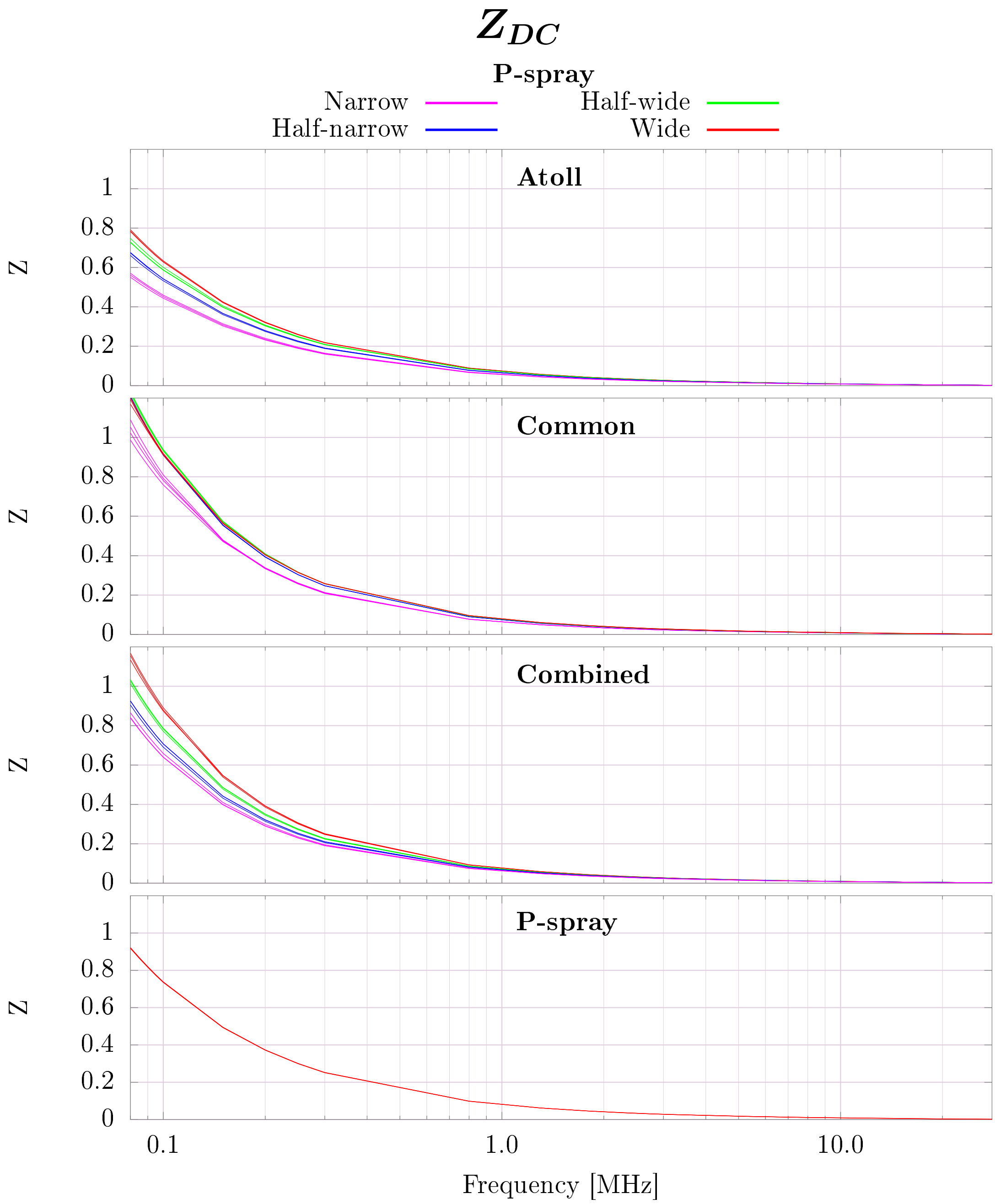

Figure 5.16: The complex impedance of the C_{DC} measurement.

5.5.4 Capacitance vs. p-stop distance

The measurements revealed the relevance of the p-stop shape for the interstrip capacitance and also its dependency to the distance d between the p-stop and strip implant. For further analysis, the average capacitance of each p-stop variation was taken, at a frequency of 1MHz and plotted against the distance d (figure 5.17 and 5.18). To gain a sensor size independent parameter the capacitance was divided by the strip length.

For each p-stop pattern a matching fit function could be found, satisfying the behavior of the C_{AC} and C_{DC} capacitance, respectively. For the combined pattern a linear fit function was appropriate:

$$g(x) = kx + l \tag{5.1}$$

With the corresponding parameter values listed below.

	C_{AC}	C_{DC}
k	-8.3 $\cdot 10^{-3}$ $\pm$ 6.8 $\cdot 10^{-5}$ (0.8 %)	-5.4 $\cdot 10^{-3}$ $\pm$ 3.1 $\cdot 10^{-4}$ (5.8 %)
l	1.244 $\pm$ 1.9 $\cdot 10^{-3}$ (0.1 %)	1.021 $\pm$ 8.5 $\cdot 10^{-3}$ (0.8 %)

Table 5.3: The fitting parameters for the combined pattern.

A polynomial fit was best for the atoll pattern,

$$f(x) = bx^2 + cx + d \tag{5.2}$$

with the following calculated parameters,

	C_{AC}	C_{DC}
b	3.5$\cdot 10^{-4}$ $\pm$ 4.4 $\cdot 10^{-5}$ (12.4 %)	1.9$\cdot 10^{-4}$ $\pm$ 8.7 $\cdot 10^{-6}$ (4.5 %)
c	-0.028 $\pm$ 2.2 $\cdot 10^{-3}$ (7.9 %)	-0.017 $\pm$ 4.4 $\cdot 10^{-4}$ (2.6 %)
d	1.490 $\pm$ 2.4 $\cdot 10^{-2}$ (1.6 %)	1.197 $\pm$ 4.9 $\cdot 10^{-3}$ (0.4 %)

Table 5.4: The fitting parameters for the atoll pattern.

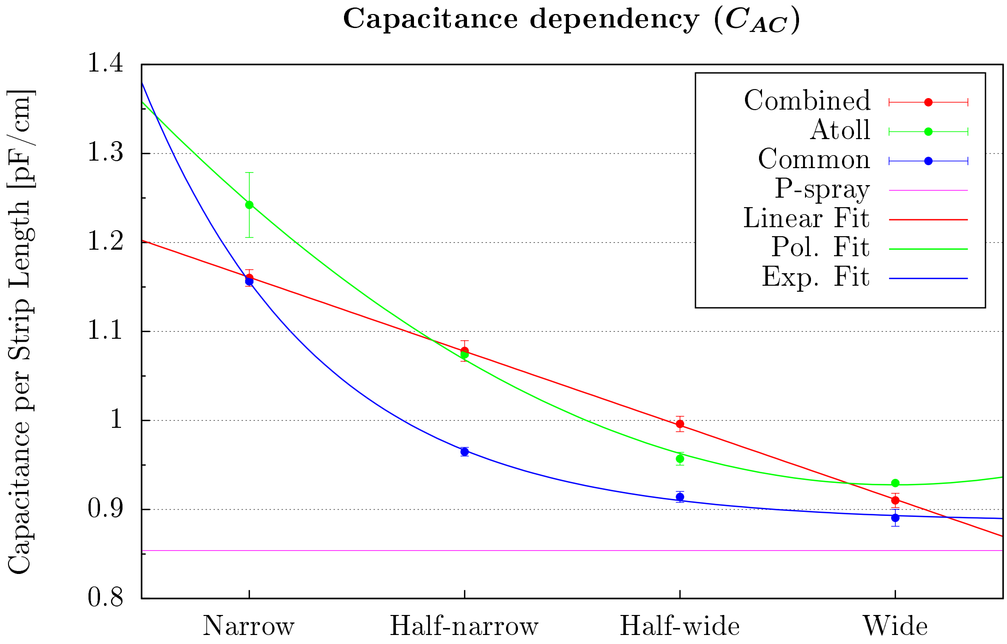

Figure 5.17: The dependency between C_{AC} and the distance between strip implant and p-stop barrier.

The common pattern showed an exponential behavior,

$$h(x) = u + v\,\mathrm{e}^{wx} \tag{5.3}$$

	C_{AC}	C_{DC}
u	$0.886 \pm 6.2 \cdot 10^{-3}$ (0.7 %)	$0.777 \pm 9.5 \cdot 10^{-3}$ (1.2 %)
v	$0.905 \pm 7.9 \cdot 10^{-2}$ (8.7 %)	$0.559 \pm 8.1 \cdot 10^{-2}$ (14.6 %)
w	$-0.121 \pm 9.9 \cdot 10^{-3}$ (8.2 %)	$-0.107 \pm 1.7 \cdot 10^{-2}$ (16.0 %)

Table 5.5: The fitting parameters for the common pattern.

For a better understanding of those dependencies, simulations had been done, which will be discussed in the next chapter.

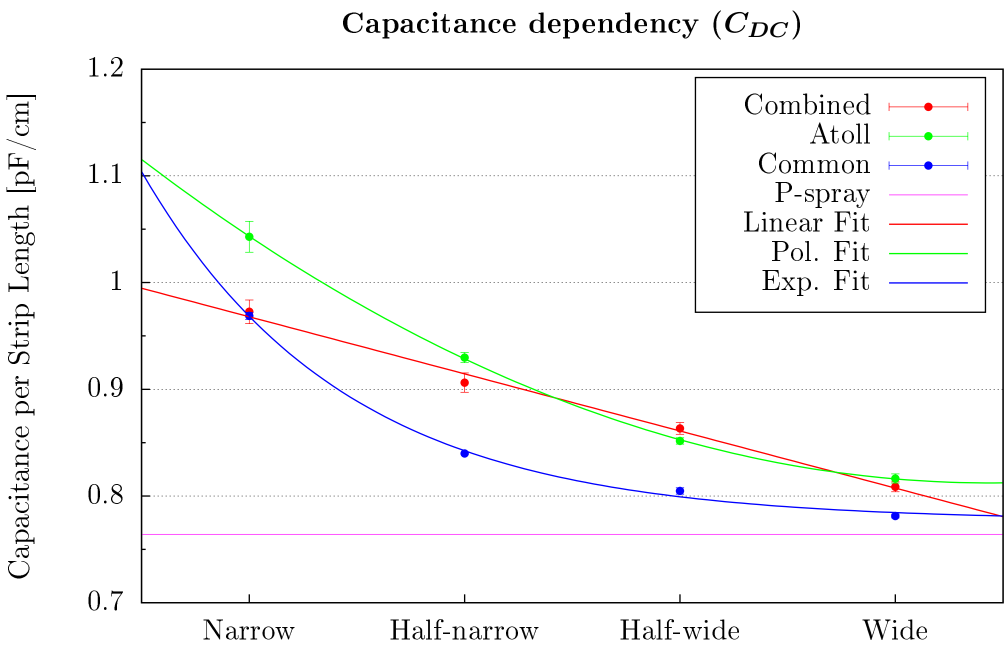

Figure 5.18: The dependency between C_{DC} and the distance between strip implant and p-stop barrier.

6 SPICE Simulations

6.1 The SPICE model

The simulation is based on a detailed circuit model of the double sided silicon sensor. The goal was to achieve a model, reflecting the measured interstrip capacities. For this purpose a complex network (see fig. 6.5) of capacitors and resistors was designed and simulated with SPICE [1] to calculate the occurring currents and voltages. The same approach was used in the references [23] and [22]. The software used for the SPICE simulation is called LTspice IV, it is a freeware from Linear Technology [2].

6.1.1 SPICE model of the LCR meter

For a proper simulation, also the LCR meter needed to be presented by an electric equivalent circuit, emulating its electrical behavior. For this purpose the model of M. A. Frautschi, M. R. Hoeferkamp and S. C. Seidel [23] was used, because their measurement device, a HP 4284A Precision LCR meter, is very similar to the here used HP 4285A. The main difference between those devices, is the supported frequency range, but their measurement principle is the same. So the SPICE model of the LCR meter was also suitable for my purposes, and is shown in figure 6.1a.

The LCR meter uses a technique called "auto balance bridge". Basically it measures the phase shift φ of an injected voltage V_{osc}, and calculates the corresponding impedance. The simulation used the same approach and calculated Z by a division of the voltage between the two input ports and the current flowing through **In2**.

$$Z = \frac{V(\mathbf{In1}) - V(\mathbf{In2})}{I(\mathbf{In2})} \tag{6.1}$$

6.1.2 Calculation of the Resistance and Capacitance

The set of formulas used for the impedance parameter calculation depend on the chosen equivalent circuit mode (The circuit modes are described in section 5.4 on page 45). The complex impedance can always be represented as,

$$Z = R + iX \tag{6.2}$$

[1]SPICE...Simulation Program with Integrated Circuit Emphasis
[2]Linear Technology: `http://www.linear.com/`

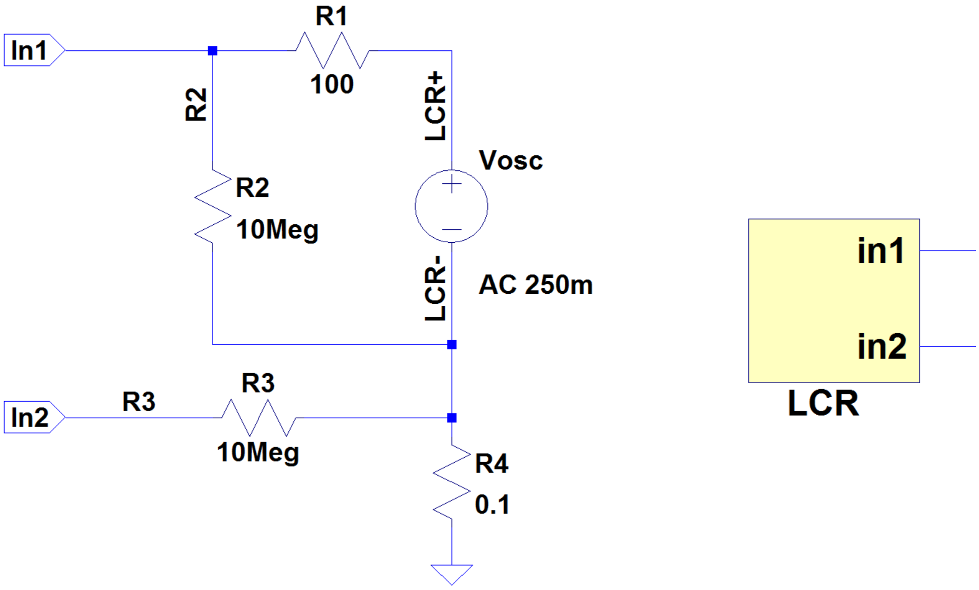

(a) Schematic view (b) Symbol

Figure 6.1: The schematic equivalent circuit of the LCR meter [23] and its subcircuit symbol used for the sensor simulations.

with the resistance R and the reactance X given as,

$$R = |Z| \cos \varphi \tag{6.3}$$
$$X = |Z| \sin \varphi \tag{6.4}$$

For the serial RC circuit mode Z is simply,

$$Z = R_S + iX_{C_S} \tag{6.5}$$

therefore,

$$R_S = R \tag{6.6}$$
$$X_{C_S} = \frac{1}{2\pi f C_S} = X \Rightarrow C_S = \frac{1}{2\pi f X} \tag{6.7}$$

with R_S the serial resistor and C_S the serial capacitance.
For the parallel model Z is given as,

$$Z = \frac{1}{\frac{1}{R_P} + i\frac{1}{X_{C_P}}} \tag{6.8}$$

With the reciprocal of eq. 6.2 and 6.8 one gets,

$$\frac{1}{Z} = \frac{R}{R^2 + X^2} - i\frac{X}{R^2 + X^2} = \frac{1}{R_P} + i\frac{1}{X_{C_P}}, \tag{6.9}$$

which leads to formulas for the parallel resistance R_P and capacitance C_P.

$$R_P = \frac{R^2 + X^2}{R} \tag{6.10}$$

$$X_{C_P} = \frac{R^2 + X^2}{X} = \frac{1}{2\pi f C_P} \Rightarrow C_P = \frac{X}{2\pi f (R^2 + X^2)} \tag{6.11}$$

For the measurements only the parallel mode was used, therefore also only eq. 6.10 and 6.11 have been used for the calculation of the simulation results.

6.1.3 SPICE model of the sensor strips

The idea behind the sensor model is to divide each strip into multiple elements. Each element is a copy of the same strip-element subcircuit with capacitors for the interstrip, backplane and coupling capacitances and with resistors for the readout and implant strip resistance 6.3.

The strip-element model was obtained from the sketch illustrated in fig. 6.2. The strip implant and the readout strip are coupled capacitive via C_C and also to their corresponding neighbors with C_{AC} and C_{DC} respectively. Furthermore, the strip implant is connected to the backplane over the backplane capacitance C_B. R_{AC} and R_{DC} meet the requirements of the readout and implant strip being no perfect conductors. R_B replaces in the model the bias resistor.

Additionally, a current source for the simulation of the dark current I_D was integrated, but as it turned out it had no impact on the capacitance simulation results.

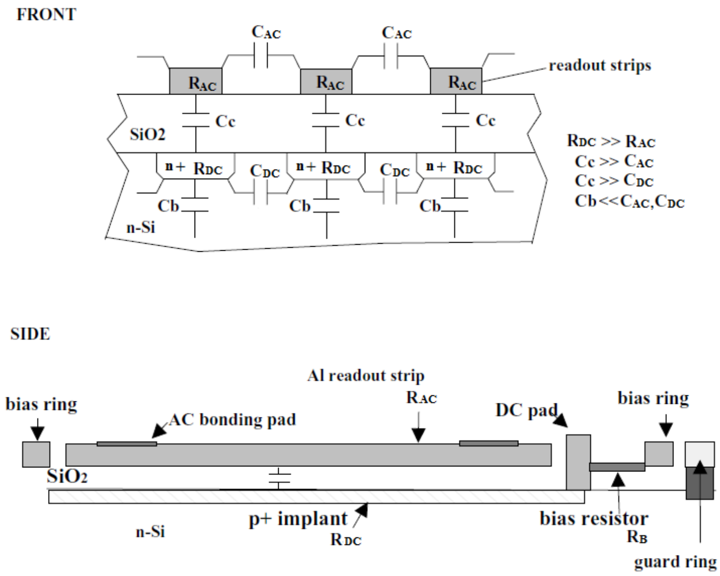

Figure 6.2: Cross sectional view of the detector, with an illustration of the electrical equivalent capacitor-resistor network. The picture was taken from M. A. Frautschi [23], with some changes to the description to match the situation of this work.

6.1.4 SPICE model of the pstop implant

During the first attempts the coupling between the implant strips was established, through a single capacitor between the neighboring strip elements. Just like the coupling between the read out strips, which is simulated by the C_{AC} capacitor inside a *Strip Element* subcircuit. This did not work out very well, so the next step I tried was to remove the C_{DC} inside the *Strip Element* subcircuit and divide the pstop-implants, like the strips, into elements. Each pstop element represents a simple subcircuit (fig. 6.4) containing the interstrip capacitance C_{DC}, for the coupling between the neighboring implant strips, and a resistors R_{pstop} for the connection between each pstop-element.

6.1.5 SPICE model of the measurement setup

The model for the simulation of the capacitance measurements used three strips, one center strip and two neighbor strips. To get a good approximation of the real sensor, the amount of elements needs to be high enough so that the natural frequencies of each element do not occur in the simulation [23]. For this simulation 10 elements per strip were used, because more elements did not significantly change the outcome.

Each DC strip was connected via a $40M\Omega$ poly-resistor to the bias line. Although a change of the bias voltage had no influence on the simulation results of the

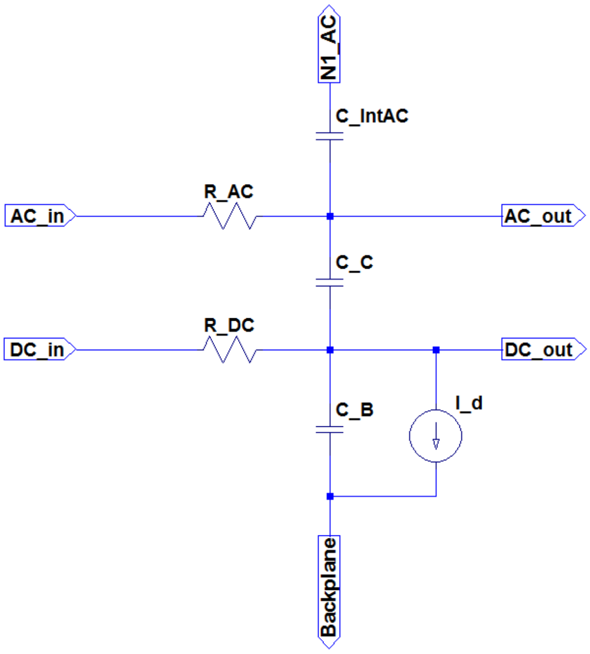

(a) Schematic SPICE model of one strip element.

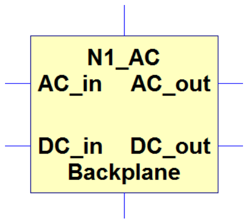

(b) Symbol

Figure 6.3: The SPICE model of one strip element.

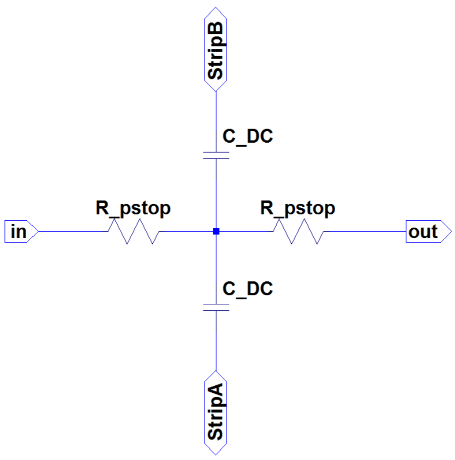

(a) Schematic SPICE model of one pstop element.

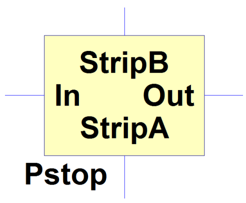

(b) Symbol

Figure 6.4: The SPICE model of one pstop element.

interstrip capacitances, it was modeled via a DC voltage source, between the bias line and the backplane (symbolized by the **Bp**-port). The neighboring AC and

DC pads are connected through ports, named "N_AC_Pad" and "N_DC_Pad" respectively. Also the connection of the LCR-meter to the circuit was established via ports, rather than with direct wiring, because so the different measurements could be done by simply renaming the ports connected to the LCR-meter.

6.1.6 Simulation parameters

The values from the coupling capacitance C_C and bias resistor R_{poly} have been taken from table 5.2. In this table C_C is given as capacitance per strip length and width, but for the simulation the capacitance per strip was needed. Therefore the $1.13\,\frac{\mathrm{pF}}{\mathrm{cm\,\mu m}}$ were multiplied with the strip implant area of $2.56\,\mathrm{cm} \times 25\,\mathrm{\mu m}$. The backplane capacitance C_B is:

$$C_B = \frac{C_{tot}}{N} \tag{6.12}$$

with C_{tot} as the total sensor capacitance and N as the amount of strips. For a fast approximation of C_B the formula for a parallel plate capacitor was taken to calculate C_{tot}:

$$C_{tot} = \epsilon_r \epsilon_0 \frac{A}{d} \tag{6.13}$$

For $\epsilon_r(Si) = 11.7$, $\epsilon_0 = 8.854 \cdot 10^{-12}\mathrm{F\,m}$, $A = 2.56\,\mathrm{cm} \times 2.56\,\mathrm{cm}$, $d = 300\,\mathrm{\mu m}$ and $N = 256$ the backplane capacitance per strip is $0.884\,\mathrm{pF}$.

For the readout strip resistors R_{AC} a thickness of $1\,\mathrm{\mu m}$ was assumed. According to [24] an Al film of this thickness has an electrical resistivity of $\rho = 3.27\,\mathrm{\mu\Omega\,cm}$. Multiplied with the form factors of the strip this yields:

$$R_{AC} = 3.27\,\mathrm{\mu\Omega\,cm} \cdot \frac{2.56\,\mathrm{cm}}{25\,\mathrm{\mu m} \cdot 1\,\mathrm{\mu m}} = 33.48\,\Omega \tag{6.14}$$

For the implant strip an electrical resistivity of $\rho = 0.03\,\Omega\,\mathrm{cm}$ was assumed, which results in a R_{DC} of about $300\,\mathrm{k\Omega}$.

Parameter	Value
R_{poly}	$40\,\mathrm{M\Omega}$
C_C	$72.32\,\mathrm{pF}$
C_B	$0.884\,\mathrm{pF}$
R_{DC}	$300\,\mathrm{k\Omega}$
R_{AC}	$33.48\,\Omega$

Table 6.1: Overview of the used values for the simulation parameters.

Please note, that all values (except R_{poly}) needed to be divided by the amount of strip elements per strip N, to get the corresponding component value. The interstrip capacitances C_{intAC} and C_{intDC} as well as the resistivity of the pstop

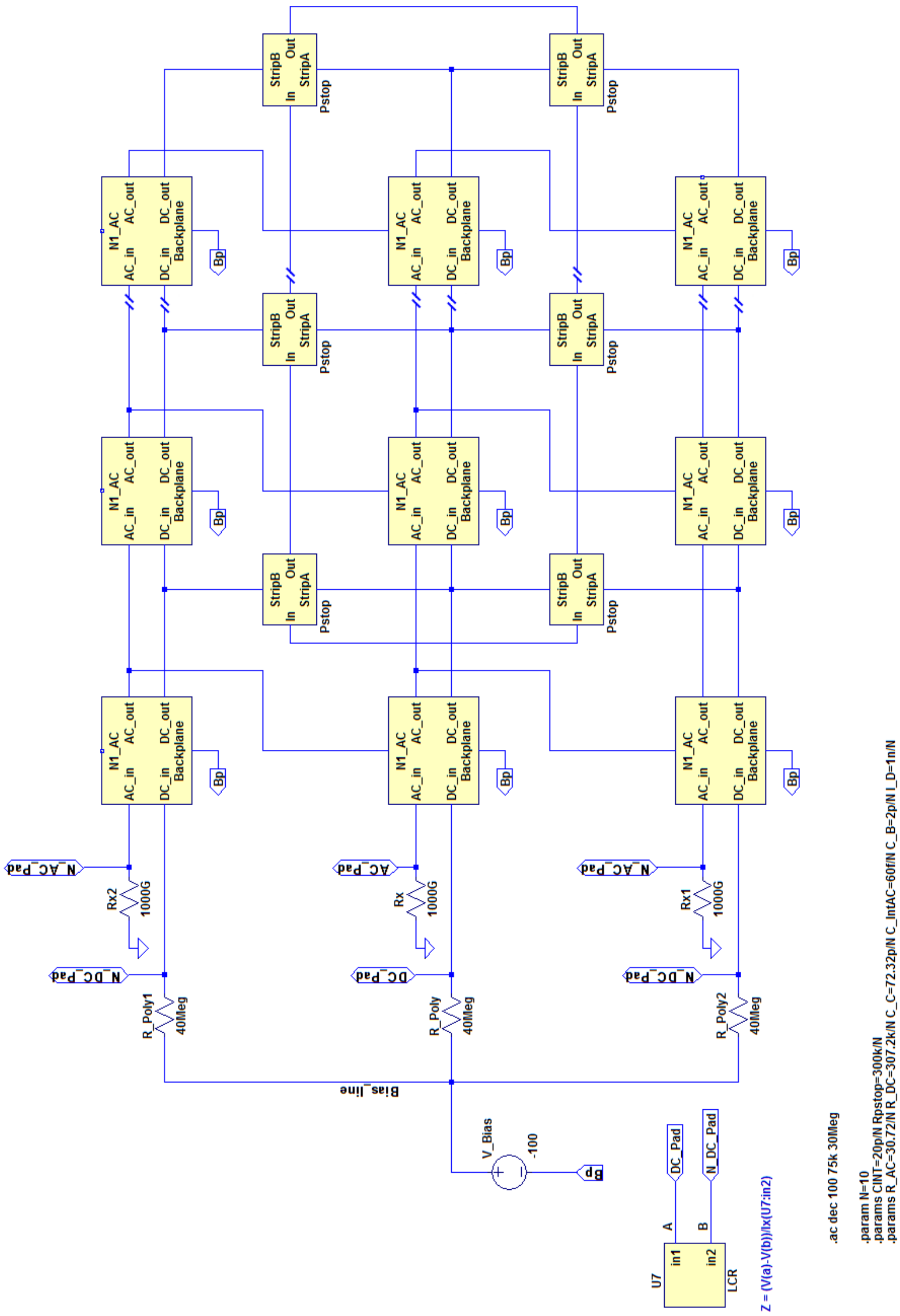

Figure 6.5: Circuit model used for the simulation of the capacitance measurements. The figure shows only 3 elements per strip, but for the real simulation 10 elements had been used. The gaps of the connection wires symbolize the missing strip and pstop elements.

barriers R_{pstop} were the only unknown parameters. In the following section, it was tried to adjust this values in such a way that the simulation and the measurement results match.

6.1.7 Simulation runs

The **.ac** spice parameter was used, to simulate the capacitance at different frequencies. This leads to a frequency sweep simulation. As frequency range the one of the HP 4285A LCR meter (75 kHz to 30 MHz) was used with a resolution of 100 points per decade.

As described in the previous section all parameters could be directly measured or were calculated, except the interstrip capacitances C_{intAC} and C_{intDC} and the pstop resistivity R_{pstop}.

During the simulation runs, it could be observed, that a variation of C_{intAC} leads to an increase of both C_{AC} and C_{DC}. Raising C_{intAC} had the same effect, but it also decreased the resistivity and cutoff frequency. Changing $R_p stop$ had neither on C_{AC} nor on C_{DC} a significant influence. However, no parameter set could be found matching the measurement results. Figure 6.6 and 6.7 show the simulation results with the parameter values from table 6.1 and with $C_{intAC} = 600\,\mathrm{fF}/N$, $C_{intDC} = 2\,\mathrm{pF}/N$, $R_{pstop} = 300\,\mathrm{k}\Omega/N$ and $N = 10$.

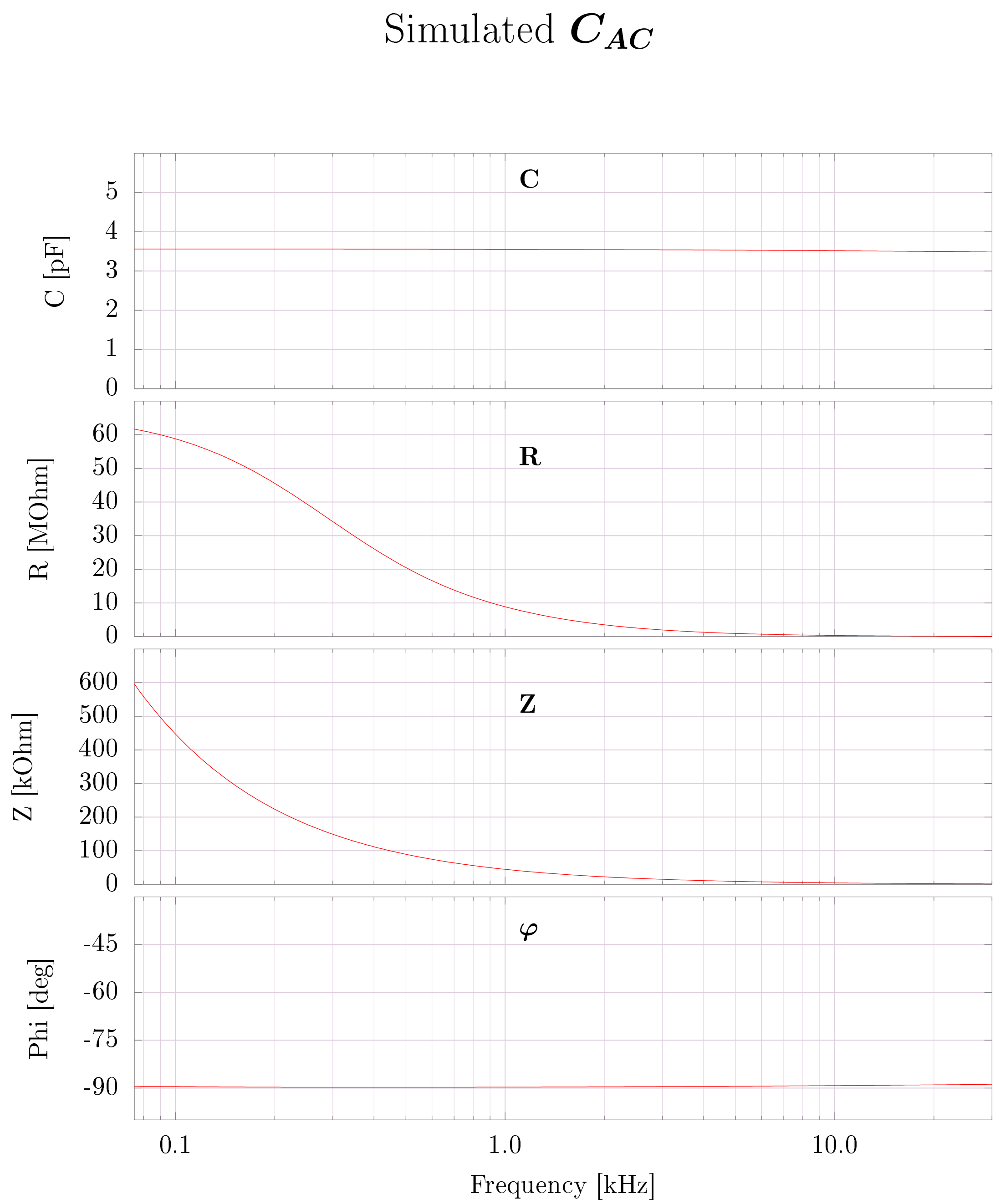

Figure 6.6: Simulation of C_{AC}

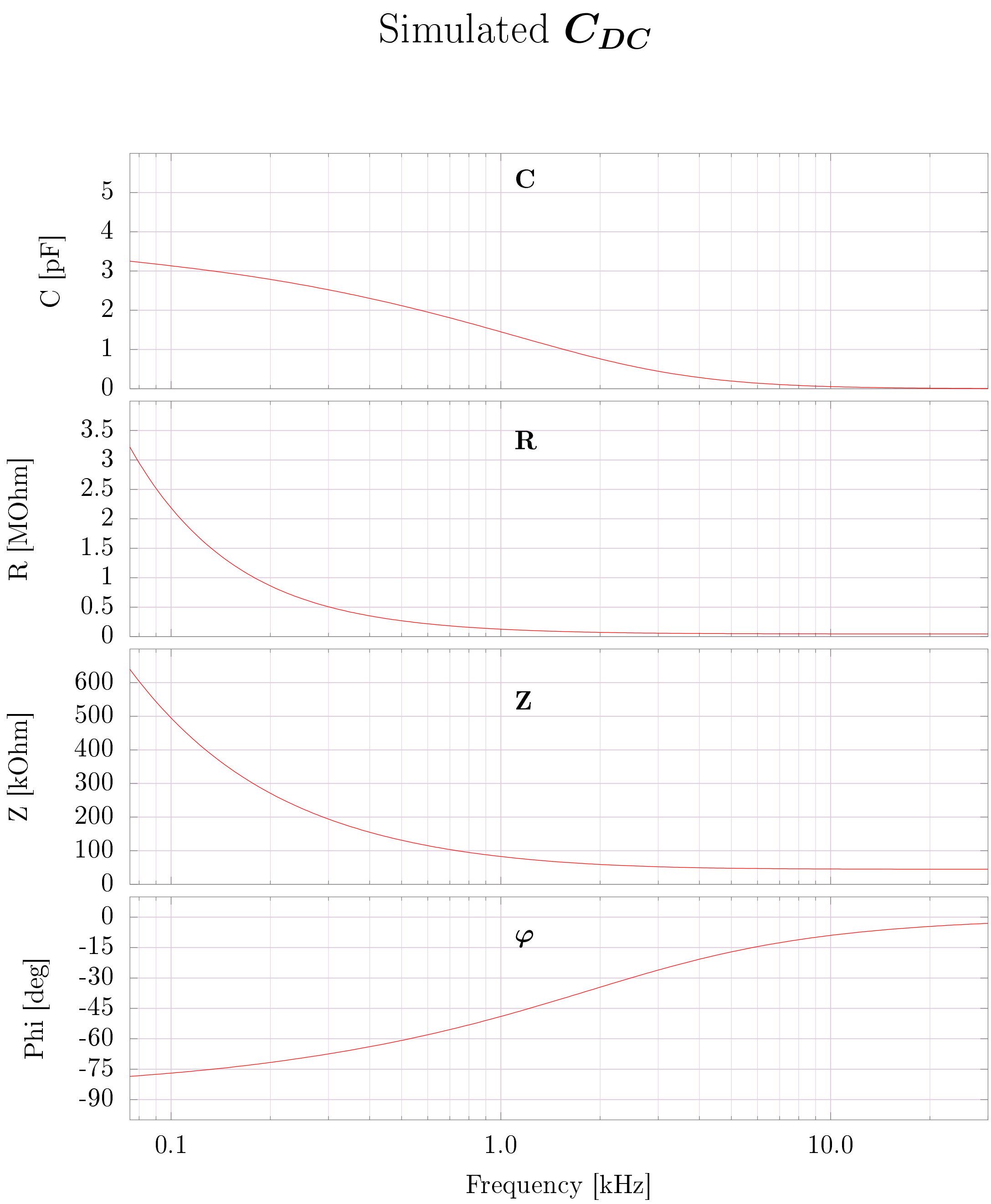

Figure 6.7: Simulation of C_{DC}

7 Conclusion and outlook

As explained in section 3.1.9 the interstrip capacitance has a major impact on the SNR. The measurements revealed, that the pspray pattern has over the whole frequency range the lowest interstrip capacitances. Nevertheless it is not the best strip insulation method, because of its bad irradiation hardness, which was examined in [13] during beam tests. In reference [13] it was also shown that the atoll pattern performs best, in comparison to the common and combined pattern. Because of that the atoll pattern was chosen for the final version of the sensor design.

An interesting capacitance dependency with regards to the distance between the strip and its p-stop barrier could be found. There the combined p-stop showed a linear, the atoll a polynomial and the common p-stop an exponential behavior. With simulations it was tried to determine the cause for this behavior, but they did not worked out as expected. Lots of different parameter sets were tested, without luck. This leads to the suspicion that the used model needs further improvements. Due to the fact, that [22] and [23] used nearly the same strip model, except the pstop element, with success for similar problems, it may be worth to study different or other approaches for the pstop model. Another simulation software like TCAD [1] may lead to more satisfying results, because it models the behavior of electrical devices based on fundamental physics.

[1] Technologie Computer Aided Design

Bibliography

[1] MissMJ. Standard Model of Elementary Particles.svg. http://commons.wikimedia.org/wiki/File:Standard_Model_of_Elementary_Particles.svg.

[2] D.R.Marlow. B-factory detectors. *Nucl. Instr. and Meth.*, A 478:80–87, 2002.

[3] Makoto Kobayashi and T Maskawa. CP-violation in the renormalizable theory of weak interaction. *Progress of Theoretical Physics*, 49(2):652–657, 1973.

[4] J W Flanagan and Y Ohnishi. Letter of Intent for KEK Super B Factory Part III : Accelerator Design. *KEK Report*, 2004.

[5] Belle II Collaboration. Belle II 3D model. http://belle2.kek.jp/images/BelleII3D+2people.pdf.

[6] J. Kemmer and G. Lutz. New detector concepts. *Nuclear Instruments and Methods in Physics Research Section A: Accelerators, Spectrometers, Detectors and Associated Equipment*, 253:365 – 377, 1987.

[7] S Uno, T Abe, I Adachi, K Adamczyk, and S Ahn. Belle II technical design report. *arXiv preprint arXiv:1011.0352*, (October), 2010.

[8] M. Krammer. Lecture: Grundlagen der Teilchendetektoren. http://www.hephy.at/lehre/.

[9] A Frankenberger. *Development of an open CO2 cooling system for Belle II.* Diploma thesis, University of Vienna, 2013.

[10] M. French, L. Jones, Q. Morrissey, A. Neviani, R. Turchetta, J. Fulcher, G. Hall, E. Noah, M. Raymond, G. Cervelli, and Others. Design and results from the APV25, a deep sub-micron CMOS front-end chip for the CMS tracker. *Nuclear Instruments and Methods in Physics Research Section A: Accelerators, Spectrometers, Detectors and Associated Equipment*, 466(2):359–365, 2001.

[11] Wolfgang Demtröder. *Experimentalphysik 3 Atome, Moleküle und Festkörper*, volume 5. Auflage. Springer-Verlag, 2005.

[12] S.M. Sze and Kwok K. Ng. *Physics of semiconductor devices.* John Wiley & Sons, third edition, 2006.

[13] Manfred Valentan. *The Silicon Vertex Detector for b-tagging at Belle II*. Dissertation, Vienna University of Technology, 2013.

[14] D. E. Groom and S. R. Klein. Passage of particles through matter. *The European Physical Journal C*, 15(1-4):163–173, March 2000.

[15] Yung-Su Tsai. Pair production and bremsstrahlung of charged leptons. *Reviews of Modern Physics*, 46(4):815–851, October 1974.

[16] K Ohmori, H Ikeda, A Sakai, S Zaima, and Y Yasuda. The Origin and the Creation Mechanism of Positive Charges in Silicon Oxide Films. *Proc. 4th Int. Symp. on the Physics and Chemistry of SiO2 and the Si-SiO2 Interface*, page 345, 2000.

[17] M Friedl. *The CMS silicon strip tracker and its electronic readout*. Dissertation, Vienna University of Technology, 2001.

[18] Cake Software Foundation. CakePHP Cookbook Documentation, Release 2.x.

[19] M. Valentan, T. Bergauer, M. Dragicevic, M. Friedl, C. Irmler, E. Huemer, and W. Treberspurg. Optimization of Strip Isolation for Silicon Sensors. *Physics Procedia*, 37:891–898, January 2012.

[20] T Bergauer. *Design, Construction and Commissioning of the CMS Tracker at CERN and Proposed Improvements for Detectors at the Future International Linear Collider*. PhD thesis, Vienna University of Technology, 2008.

[21] Agilent Technologies. Agilent 4285A Precision LCR Meter - Operation Manual. (March):523, 2000.

[22] E Barberis, N Cartiglia, and C LeVier. Capacitances in silicon microstrip detectors. *Nucl. Instr. and Meth.*, 342:90–95, 1994.

[23] M.A. Frautschi, M.R. Hoeferkamp, and S.C. Seidel. Capacitance measurements of double-sided silicon microstrip detectors. *Nuclear Instruments and Methods in Physics Research Section A: Accelerators, Spectrometers, Detectors and Associated Equipment*, 378(1-2):284–296, August 1996.

[24] F. Avilés, O. Ceh, and A. I. Oliva. Physical properties of Au and Al thin films measured by resistive heating. *Surface Review and Letters*, 12(01):101–106, February 2005.

List of Figures

Bernhard Leitl

Ausbildung

1996-2000 Lerchenfeld Gymnasium

- *Schwerpunkt Italienisch*

2000-2005 HTL Mössingerstraße Klagenfurt

- *Technische Informatik*
- *Maturaabschluss 26.Juli 2005*

2006-2014 Universität Wien Wien

- *Bachelor-/Masterstudium Physik*